

# Decreasing seasonal cycle amplitude of methane in the northern high latitudes being driven by lower latitude changes in emissions and transport

Emily Dowd<sup>1</sup>, Chris Wilson<sup>1,2</sup>, Martyn P. Chipperfield<sup>1,2</sup>, Emanuel Gloor<sup>3</sup>, Alistair Manning<sup>4</sup>, and Ruth Doherty<sup>5</sup>

<sup>1</sup>School of Earth & Environment, University of Leeds, Leeds, UK

<sup>2</sup>National Centre for Earth Observation, University of Leeds, Leeds, UK

<sup>3</sup>School of Geography, University of Leeds, Leeds, UK

<sup>4</sup>Met Office, Exeter, UK

<sup>5</sup>School of GeoSciences, University of Edinburgh, Edinburgh, UK

**Correspondence:** Emily Dowd (eed@leeds.ac.uk)

**Abstract.** Atmospheric methane (CH<sub>4</sub>) concentrations are rising which is expected to lead to a corresponding increase in its global seasonal cycle amplitude (SCA), the difference between its seasonal maximum and minimum values. The reaction between CH<sub>4</sub> and its main sink, OH, is dependent on the amount of CH<sub>4</sub> and OH in the atmosphere. The concentration of OH varies seasonally and due to the increasing burden of CH<sub>4</sub> in the atmosphere, it is expected that the SCA of CH<sub>4</sub> will increase due increased removal of CH<sub>4</sub> through reaction with OH in the atmosphere. Spatially-varying changes in the SCA could indicate long-term persistent variations in the seasonal sources and sinks but such SCA changes have not been investigated. Here we use surface flask measurements and a 3-D chemical transport model (TOMCAT) to diagnose changes in the SCA of atmospheric CH<sub>4</sub> between 1995-2020 and attribute the changes regionally to contributions from different sectors. We find that the observed SCA decreased by 4 ppb (7.6%) in the northern high latitudes (NHL, 60°N-90°N), whilst globally the SCA increased by 2.5 ppb (6.5%) during this time period. TOMCAT reproduces the change in the SCA at observation sites across the globe. Therefore, we use it to attribute regions which are contributing to the changes in the NHL SCA, which shows an unexpected change in the SCA that differs to the rest of the world. We find that well-mixed background CH<sub>4</sub>, likely from emissions originating in, and transported from, more southerly latitudes has the largest impact on the decreasing SCA in the NHL (56.5% of total contribution to NHL). In addition to the background CH<sub>4</sub>, recent emissions from Canada, the Middle East and Europe contribute 16.9%, 12.1% and 8.4%, respectively, to the total change in the SCA in the NHL. The remaining contributions are due to changes in emissions and transport from other regions. The three largest regional contributions are driven by increases in summer emissions from the Boreal Plains in Canada, decreases in winter emissions across Europe, and a combination of increases in summer emissions and decreases in winter emissions over the Arabian Peninsula and Caspian Sea in the Middle East. These results highlight that changes in the observed seasonal cycle can be an indicator of changing emission regimes in local and non-local regions, particularly in the NHL where the change is counter-intuitive.

## 1 Introduction

Methane ( $\text{CH}_4$ ) is the second most important anthropogenic greenhouse gas in the atmosphere after carbon dioxide ( $\text{CO}_2$ ) and anthropogenic emissions have contributed an extra 23% to the radiative forcing in the troposphere since 1750 (Saunio et al., 2020). Global observations by the National Oceanic and Atmospheric Administration (NOAA) Earth System Research Laboratories (ESRL) show that concentrations of atmospheric  $\text{CH}_4$  have risen since the 1980s, with a short hiatus in the growth between 1999 and 2006. Our understanding of the drivers of the global trends of  $\text{CH}_4$  remains incomplete (Nisbet et al., 2016, 2019; Dlugokencky et al., 2021). Long-term trends of  $\text{CH}_4$  are monitored through surface flask observations by NOAA ESRL and have been studied extensively. Long-term variations in the seasonal cycle of  $\text{CH}_4$  have not been analysed in detail since a study by Dlugokencky et al. (1997), although several studies have briefly discussed its seasonal cycle (e.g. Pickett-Heaps et al. (2011); Bergamaschi et al. (2018); Patra et al. (2011); Parker et al. (2020)).

$\text{CH}_4$  has a mixture of natural and anthropogenic sources and chemical sinks which lead to a strong seasonal cycle in the atmosphere. Figure 1 shows the mean seasonal cycle across NOAA observation sites (Table 1) in the northern and southern hemispheres, where concentrations are at a minimum in summer and peak in winter or early spring, depending on location. The atmospheric  $\text{CH}_4$  seasonal cycle is driven by the seasonal variations of sources such as wetlands, rice paddies and biomass burning, the chemical loss of  $\text{CH}_4$  in the atmosphere, and the transport of  $\text{CH}_4$ . The main sources which drive the  $\text{CH}_4$  cycle are dependent on climatological and meteorological conditions. Emissions from wetlands and rice paddies vary seasonally with changes in temperature, precipitation and soil moisture. Biomass burning emissions in the tropics and boreal regions also vary seasonally (Dlugokencky et al., 1997). It is thought that anthropogenic emissions play a smaller role in the seasonal cycle of  $\text{CH}_4$  (e.g. Meirink et al. (2008); Wilson et al. (2021)) but few studies have investigated the long-term influence of anthropogenic emissions on the observed seasonal cycle. For example, anthropogenic emissions might increase in winter due to increased gas extraction (Nisbet et al., 2019). The sinks of  $\text{CH}_4$  also play a large role in the seasonal cycle. The main sink of  $\text{CH}_4$  is the hydroxyl radical (OH) which is photochemically produced, which results in the local abundance of OH varying seasonally due to the availability of UV radiation. Finally, transport of  $\text{CH}_4$  in the atmosphere through advection, convection and global circulation transporting air to the poles also influences the seasonal cycle.

Many studies have assessed how well wetland models and chemical transport models reproduce the observed  $\text{CH}_4$  seasonal cycle, the timing of the seasonal maximum and seasonal minimum, or what might be driving the seasonal cycle on a regional scale (Patra et al., 2011; Bergamaschi et al., 2018; Parker et al., 2020). These studies did not explore how the seasonal cycle amplitude (SCA) has changed over time on a global scale. The SCA is defined as the difference between the annual maximum and the annual minimum concentration at a particular location. Changes in the seasonality of emissions will be reflected in the seasonal cycle amplitude of  $\text{CH}_4$  and will ultimately impact the annual growth rate. However, changes in loss rates and transport add extra complexity to assessing changes in the seasonal cycle. Studying the SCA could give us a better insight into changes in the  $\text{CH}_4$  budget. In this study we regionally attribute the change in SCA of  $\text{CH}_4$  between 1995-2020 using the

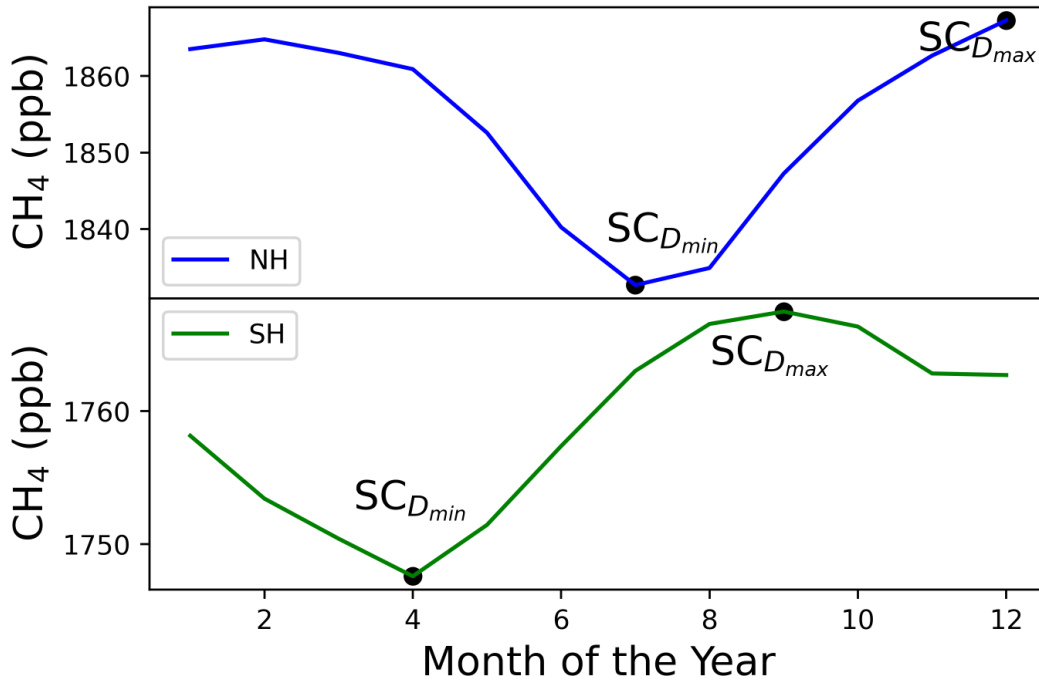


**Figure 1.** The monthly mean CH<sub>4</sub> mixing ratio (ppb) across northern hemisphere (NH) and southern hemisphere (SH) at 22 NOAA surface sites between 1995-2022 (see Table 1).  $SC_{D_{max}}$  and  $SC_{D_{min}}$  represent the seasonal cycle maximum and minimum, respectively.

55 TOMCAT chemical transport model (Chipperfield, 2006) and surface observations from NOAA ESRL (Dlugokencky et al., 2021).

Note that throughout this text we are referring to concentrations when we use "CH<sub>4</sub>" alone. In Sect. 2 we describe the observations used, the modelling methodology and the SCA analysis. In Sect. 3 and Sect. 4 we present our results and discuss our findings.

## 2 Methods

### 60 2.1 Atmospheric Methane Measurements

We assimilate and analyse the long-term surface flask measurements provided by NOAA ESRL. The air samples are collected approximately weekly or biweekly and CH<sub>4</sub> is measured using gas chromatography with flame ionization detection or by cavity ring-down spectroscopy methods (Dlugokencky et al., 2021). The NOAA observation network provides measurements across the globe, but there is a disproportionate number of sites in the northern hemisphere compared with the southern hemisphere, see Fig. 2. There is also a lack of regular observations in some tropical regions, where there are large and uncertain CH<sub>4</sub> emissions.

We assimilate NOAA surface observations in INVICAT, the inverse model of TOMCAT, in order to get optimised estimates of CH<sub>4</sub> fluxes to use in the TOMCAT forward model. We used observations from 80 NOAA surface observation sites and assimilated them at the correct model time step. Full details of the assimilation can be found in Sect. 2.3. In the SCA analysis we used a subset of these observations. We calculated the monthly mean CH<sub>4</sub> at 22 NOAA surface sites which were selected if they contained observations for the entire period 1995-2020 and were not strongly influenced by local sources (McNorton et al., 2018). A list of the sites and their site codes are in Table 1 and their locations are shown by the blue dots in Fig. 2. We also evaluate the model performance using observations from the Center for Global Environmental Research Earth System Division, National Institute for Environmental Studies, Japan (NIES, Tohjima et al. (2002); Sasakawa et al. (2010)) and the Advanced Global Atmospheric Gases Experiment (AGAGE, Prinn et al. (2018)) which have not been assimilated, see Supplement Fig. S1. The sites from NIES are in Siberia and East Asia and the site from AGAGE is situated in Ireland, their locations are shown as the red dots in Fig. 2. The independent observations do not cover the whole study period but we have maximised the time period available from each data set by selecting a period with the most regular observations. The NIES observations in Siberia are from 2009-2015, the remaining NIES observations are from 1997-2015 and the AGAGE observations are from 1996-2020.

## 2.2 Tagged Transport Simulations

TOMCAT is a three-dimensional (3D) atmospheric chemical transport model which has been used in a number of studies to model CH<sub>4</sub> and other chemical species in the atmosphere (e.g. Chipperfield (2006); Parker et al. (2018); Wilson et al. (2021)). We use TOMCAT to investigate changes in the SCA of CH<sub>4</sub> between 1995 and 2020, including the impact of changes in emissions and transport. The globe was divided into 18 different regions, shown in Fig. 2, in order to attribute the changes in the SCA from particular regions. The regions were selected based on the magnitude and type of emission in the distribution used in TOMCAT. The northern oceans, Greenland, Iceland and Svalbard have been grouped together (North Oceans and Arctic, NOA), as were the southern oceans and Antarctica (SOA). Northern land regions have been split into Canada (CAN), Europe (EUR) and Russia (RUS) due to their emissions types and geographical location. The emissions from these regions include anthropogenic emissions such as those from oil and gas industries, livestock and other agriculture, but also include natural emissions such as those from wetlands and biomass burning. In the northern mid-latitudes regions such as North America (NAM), Middle East (ME) and China & Japan (CHJA) are dominated by large anthropogenic emissions. Africa has been split into three regions because of the influence of central Africa in the CH<sub>4</sub> budget, with recent studies highlighting the large role tropical wetlands play in the recent global growth (Lunt et al., 2021; Feng et al., 2022). Similarly, Brazil has been split into three regions due to the local emission sectors and different responses to seasonal changes in meteorology (Wilson et al., 2021; Basso et al., 2021). The North Brazil (NBRA) emissions are mostly driven by wetlands, whereas East Brazil (EBRA) is more susceptible to biomass burning in the arc of deforestation, a region of regular and intense anthropogenic burning. The South Brazil (SBRA) emissions are driven by a mixture of both wetlands and biomass burning. The rest of South America has been grouped as Non-Amazon South America. Emissions from the South East Asia region (SEA) is from a mixture of rice paddies, biomass burning and other anthropogenic emissions, whilst Australia (AUS) is mostly driven by anthropogenic emissions, such as those from coal mines. The names given to each region are given in Table 2.

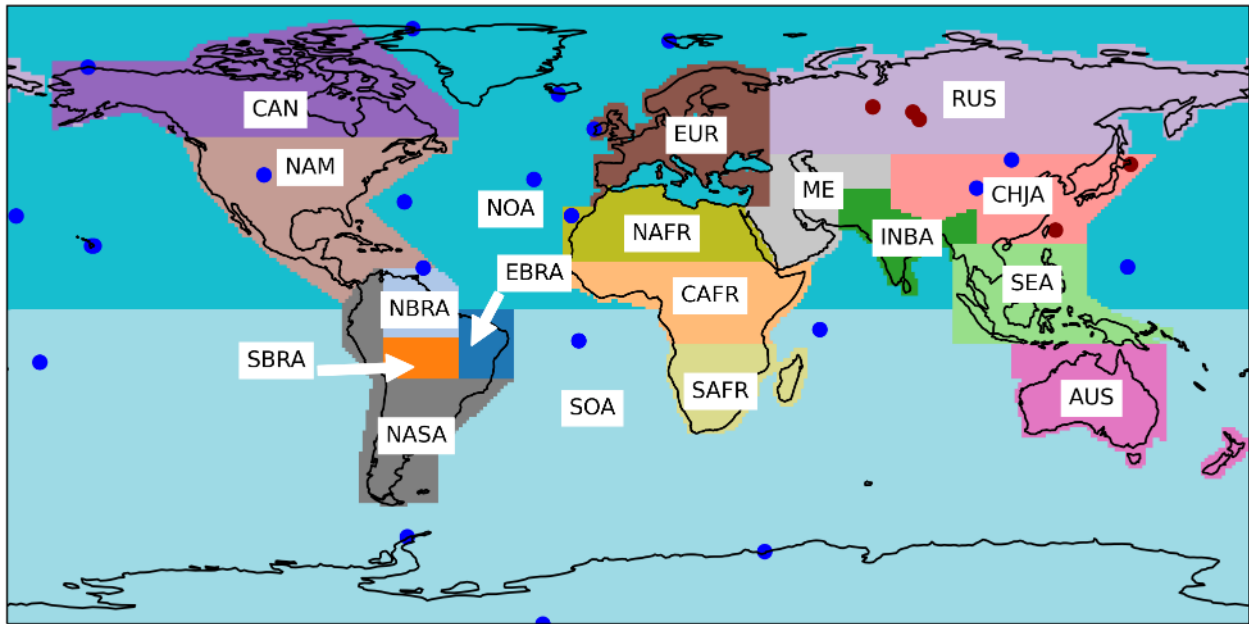


**Figure 2.** A map showing the 18 different regions selected for the tagged tracers, 22 NOAA surface observation site locations (blue) and the independent observations site locations (red). The observation sites shown are the ones used to calculate SCA from 1995-2020.

Emissions from each region were simulated separately in the model and could be summed to represent global CH<sub>4</sub>. This is possible due to the linearity of the TOMCAT model transport (Wilson et al., 2016) and offline (non-interactive) loss rates. In reality, the loss of CH<sub>4</sub> is not linear because the abundance of CH<sub>4</sub> impacts its rate of loss due to its impact on OH abundance, but this is a small effect relative to the large CH<sub>4</sub> abundance.

105 TOMCAT was run at a  $5.6^\circ \times 5.6^\circ$  horizontal resolution with 60 vertical levels up to 0.1 hPa, between 1983 and 2020 for each regional tagged tracer, a background tracer and a total CH<sub>4</sub> tracer. The background tracer contains CH<sub>4</sub> from the regional tracers once the CH<sub>4</sub> from each region has become well-mixed. Each regional tagged tracer was set to be reallocated into the background tracer using an exponential 9-month decay rate. Typical timescales for horizontal transport in the troposphere from the mid latitudes to the poles is approximately 1-2 months and interhemispheric transport is approximately 1 year (Jacob, 110 1999). The 9-month decay rate was selected in order to maximise the opportunity for CH<sub>4</sub> to undergo long-range transport from emission locations to surface sites, whilst minimising the effect of well-mixed atmospheric CH<sub>4</sub> on the results. The background tracer allows us to reduce the spin-up time required in the model to reach steady state. Without the background allocation concentrations would continue to increase because it takes approximately 20 years for the CH<sub>4</sub> to reach steady state in the model. The background tracer also allows us to regionally attribute changes in the SCA whilst accounting for well-mixed 115 CH<sub>4</sub>.

The study period begins in 1995 to allow the tracers to become well-mixed in the preceding 12 years. This model simulation is called TOM\_regional and uses surface fluxes derived from a TOMCAT-based atmospheric inversion described in Sect. 2.3. The meteorology was driven by the European Centre for Medium-Range Weather Forecasts (ECMWF) ERA5 reanalyses (Hersbach et al., 2020) and the OH fields for the troposphere and stratosphere were based on those within the TransCom CH<sub>4</sub> study (Patra et al., 2011). The OH fields were originally taken from Spivakovsky et al. (2000) and scaled downwards by 8% in accordance with Huijnen et al. (2010) in order to match the observed methyl chloroform concentrations in the atmosphere (Patra et al., 2011). The stratospheric loss rates for Cl and O(<sup>1</sup>D) varied annually and were taken from a previous full chemistry TOMCAT simulation (Monks et al., 2017). The soil sink was taken from the MeMo model which varied each year between 1990 to 2009, the 1990 values were annually repeated from 1983-1990 and similarly, the 2009 values were repeated annually from 2009-2020 (Murguia-Flores et al., 2018).

We carried out two sensitivity experiments to investigate the impact of the choice of the exponential lifetime used to allocate well-mixed CH<sub>4</sub> into the background tracer, and if it influences the background tracer's contribution to the change in the SCA. Decay rates of 1 and 12 months were selected to show the impact of a short and long decay timescales on the background and regional contributions of the change in the SCA. The simulations are labelled TOM\_one for the 1-month decay rate and TOM\_twelve for the 12-month rate. The results of the sensitivity experiments can be found in Sect. 3.5.

The TOM\_regional simulation quantifies the impact regional emissions have on the SCA of CH<sub>4</sub> elsewhere under annually varying transport processes. In order to investigate the role that those transport processes alone play in the change in SCA of CH<sub>4</sub>, we also carried out a separate regional tagged tracer simulation using annually-repeating emissions for the same time period. Using annually-repeating values removes the influence of changing emissions, allowing us to investigate changes to the transport undergone by emissions from each region over time. The surface emissions for each month of the year were averaged between 1983-2020. These emissions were repeated annually using the same model set-up as TOM\_regional and the same analysis of SCA was repeated for 1995-2020. This constant emissions simulation is labelled TOM\_transport. A summary of the TOMCAT simulations can be found in Table 3.

### 2.3 Fluxes from Atmospheric Inversions

The surface fluxes for the tagged tracer simulations were derived using the TOMCAT-based inverse model, INVICAT (Wilson et al., 2014). INVICAT has been used in a number of studies to constrain emissions of various species, including CH<sub>4</sub> (Gloor et al., 2018; Wilson et al., 2021). It uses a 4D-Var variational method based on that used in Numerical Weather Prediction, with full details on the methods used in INVICAT given in Wilson et al. (2014). The inverse method aims to minimise the value of a cost function, in a least-squares sense. The cost function combines an error-weighted sum of the differences between the model and observations and the uncertainty-weighted sum of changes to the a priori flux estimate (Wilson et al., 2021). The input for INVICAT includes an a priori mean flux value for each grid cell and an error covariance matrix containing the covariances between the flux uncertainties. The output is an a posteriori mean grid cell flux and error covariance matrix. The a priori and a posteriori fluxes will hence be referred to as prior fluxes and posterior fluxes, respectively.

The inverse model simulations were run at a  $5.6^\circ \times 5.6^\circ$  horizontal resolution with 60 vertical levels up to 0.1 hPa and a time  
150 step of 30 min. The meteorology was taken from ECMWF's ERA5 reanalyses (Hersbach et al., 2020). An inversion was carried  
out separately for each year and completed 40 minimisation iterations. The 40 iterations were sufficient for the cost function  
and its gradient norm to be judged as converged, based on both being smaller than 1% of their initial value. The inversion for  
each year was run for 14 months, until February the following year, in order to better constrain the fluxes in the final months  
of each year. The final 2 months of each are discarded from the results. Each inversion overlapped with the following one by  
155 2 months to give the transport of fluxes time to reach measurement sites. The overlapping months were initialised using 3-D  
fields provided from the correct date in the previous year so the total CH<sub>4</sub> burden was conserved across each year.

The 4D-Var-simulated CH<sub>4</sub> mixing ratios were linearly interpolated to the correct longitude, latitude and altitude of each  
surface observation used in the inversion at the nearest model time step. The surface observations were given uncorrelated  
errors of 3 ppb plus a representation error. The representation error was estimated as the mean difference across eight grid cells  
160 around the cell which contained the observation. The prior emissions were taken from various inventories. The anthropogenic  
emissions were taken from EDGARv5 (Crippa et al., 2021), excluding rice paddies and fires. The biomass burning emissions  
were taken from GFEDv4.1s (Randerson et al., 2017). The WetCHARTS model (Bloom et al., 2017) in a median set-up was  
used for the wetland fluxes. The median set-up uses the median scaling factor and temperature response from the WetCHARTS  
suite and the Global Lakes and Wetlands Database distribution of wetlands. The wetland fluxes were then masked to remove  
165 emissions which overlap with rice emissions and then scaled back up to 180 Tg to match the top-down mean value from the  
Global Methane Budget (Saunois et al., 2020). The rice and termite emissions were taken from the Transcom intercomparison  
project (Patra et al., 2011). The termite emissions were scaled to match the total quoted in Saunois et al. (2020). The geological  
emissions were from Etiope et al. (2019) and the ocean emissions are taken from Weber et al. (2019). The prior emissions are  
given cell uncertainties of 250% of the prior flux value but also include 500 km spatial correlations with a Gaussian distribution  
170 for all fluxes. Fossil fuel fluxes have temporal correlations based on an exponential distribution with a time scale of 9 months.  
The tropospheric and stratospheric loss rates are the same as those used in the TOMCAT tagged tracer simulations (Sect. 2.2).

## 2.4 Data Processing and Analysis

The monthly mean model output from TOMCAT was interpolated horizontally and vertically to the 22 surface observation  
sites (Table 1) from NOAA's ESRL (Dlugokencky et al., 2021) to check model performance and in order to investigate the  
175 regional contribution to the change in SCA at these sites. Following methods used by Lin et al. (2020) for CO<sub>2</sub>, the seasonal  
cycle amplitude (SCA) of CH<sub>4</sub> and the regional contribution to the SCA was analysed.

To calculate the SCA, we isolate the mean annual cycle observed in CH<sub>4</sub> by taking the interpolated model output at each  
surface observation site and then smooth and detrend the time series using the CCGCRV curve-fitting routine, developed  
by Thoning et al. (1989). CCGCRV approximates the seasonal cycle and long-term trend variation by fitting a polynomial  
180 equation combined with a harmonic function (Pickers and Manning, 2015). The short-term and long-term cut off values can  
be selected and we chose 80-day and 667-day cut offs, respectively Dlugokencky et al. (1994). These parameters have been  
used in previous studies (Dlugokencky et al., 1994; Parker et al., 2018). The SCA for the observations and the modelled total

tracer was calculated by taking the difference between the annual maximum ( $SC_{D_{max}}$ ) and annual minimum ( $SC_{D_{min}}$ ) of the detrended curve:

$$185 \quad SCA = SC_{D_{max}} - SC_{D_{min}} \quad (1)$$

where  $D_{max}$  and  $D_{min}$  are the days of the annual  $CH_4$  cycle maximum and minimum. For each tagged regional tracer,  $i$ , a pseudo SCA ( $SCA'_i$ ) was calculated where the pseudo maximum ( $SC'_{i,D_{max}}$ ) or minimum ( $SC'_{i,D_{min}}$ ) is the point of its annual cycle corresponding to  $D_{max}$  and  $D_{min}$ . The pseudo seasonal cycle amplitude was calculated as:

$$SCA'_i = SC'_{i,D_{max}} - SC'_{i,D_{min}} \quad (2)$$

190 The pseudo SCA was defined to account for the difference in timing of the local  $D_{max}$  and  $D_{min}$  of the individual tracers and observed  $CH_4$  at the observation sites. The total change in SCA over the study period,  $\Delta SCA$  (ppb), was derived by calculating the linear trend ( $k_{SCA}$ ) in the SCA and multiplying it by the number of years in the study ( $n_{year}$ , 25 years):

$$\Delta SCA = k_{SCA} \times n_{year} \quad (3)$$

Once the SCA and  $\Delta SCA$  were calculated the surface sites were then grouped into five latitude bands for further analysis. 195 These groups are Northern High Latitudes (NHL, 60°N-90°N), Northern Mid Latitudes (NML, 30°N-60°N), Northern Tropics (NTr, 0°-30°N), Southern Tropics (STr, 0°-30°S) and Southern High Latitudes (SHL 60°S-90°S). There are no surface observations from the Southern Mid Latitudes (SML, 30°S-60°S) so we do not analyse the SCA in this latitude band.

The main sink of  $CH_4$  is through reaction with OH and the rate of removal is dependent on temperature and the amount of  $CH_4$  and OH in the atmosphere (Dlugokencky et al., 1997). The atmospheric burden of  $CH_4$  has been increasing and it 200 is expected that the SCA of  $CH_4$  would increase due to more  $CH_4$  being removed by OH in the atmosphere, assuming that OH concentrations remain relatively constant during this time. To account for the impact of OH on  $\Delta SCA$  we calculated the amount of  $CH_4$  lost by OH across the whole atmosphere in each month of the study period:

$$L_{CH_4} = m_{CH_4}(1 - e^{-k[OH]\Delta t}) \quad (4)$$

$$k = 2.45 \times 10^{-12} e^{(-1775/T)} \quad (5)$$

205 Where  $L_{CH_4}$  is the amount of  $CH_4$  lost (kg) in each model grid box through the reaction with OH in one month and  $m_{CH_4}$  is the mass of  $CH_4$  in kg in each grid box. The variable  $k$  is the reaction rate constant (in  $cm^3 \text{molecules}^{-1} \text{s}^{-1}$ , Equation 5 where  $T$  is temperature in Kelvin),  $[OH]$  is the amount of OH ( $\text{molecules cm}^{-3}$ ) and  $\Delta t$  is number of seconds in one month.



$L_{CH_4}$  was converted to ppb and a mean monthly loss was calculated for the northern and southern hemisphere, across all the vertical model levels over the study period. The loss was then smoothed and detrended using the CCGCRV curve fitting routine and  $\Delta SCA$  was calculated using the same method described above. It is not realistic to account for the contribution to  $\Delta SCA$  from loss by OH at individual surface sites because this would not capture the seasonal cycle of OH in the mid-troposphere, where the majority of  $CH_4$  loss by OH occurs. This makes it difficult to relate the seasonal changes in  $CH_4$  due to loss by OH at particular sites, hence why we have calculated  $L_{CH_4}$  as a mean across the northern and southern hemispheres.

### 3 Results

#### 215 3.1 Observed $\Delta SCA$

The observed  $\Delta SCA$  was calculated at the 22 observations sites. We find that the global mean SCA at available sites is increasing but there are different regional trends, for example in the NHL the observed  $\Delta SCA$  decreased at all sites between 1995-2020 (Fig. 3). The observed global mean value of  $\Delta SCA$  was 2.5 ppb, corresponding to an increase of the SCA by 6.5%. The reaction between  $CH_4$  and OH is dependent on the amount of  $CH_4$  available in the atmosphere. The combination of the increasing  $CH_4$  burden in the atmosphere and the photochemically-driven seasonal variation of OH results in more  $CH_4$  being removed from the atmosphere during the time of maximum OH. Therefore, an increase in the global mean SCA is expected due to the increasing atmospheric burden of  $CH_4$ . However, when we look at the  $\Delta SCA$  latitudinally, there are large differences in the NHL compared to the rest of the world. The mean observed  $\Delta SCA$  in the NHL was -4.0 ppb, which represents a 7.6% decrease between 1995 and 2020, and in the Non-NHL region the mean observed value of  $\Delta SCA$  was 4 ppb, which is an increase of 11.5% for the study period. The reasons for this widespread contrasting behaviour in the NHL compared to the rest of the world is investigated in more detail in the forthcoming sections.

The distribution of  $\Delta SCA$  at sites in Non-NHL regions is quite variable. For example at NWR, AZR and GMI  $\Delta SCA$  is large and positive but other sites such as MHD, IZR and SMO have negative  $\Delta SCA$  values. The sites with the largest positive  $\Delta SCA$  (e.g. NWR, BMW and AZR, GMI and WLG) are most likely influenced by outflow from the USA and Asia. The sites with large positive  $\Delta SCA$  and negative  $\Delta SCA$  in the Non-NHL regions do not have a strong regional or local pattern in  $\Delta SCA$ , unlike in the NHL. All four sites in the NHL display contrasting behaviour and have a negative  $\Delta SCA$  compared to the rest of the world therefore; the NHL will be the main focus of our analysis.

BRW, ALT and ZEP have a  $\Delta SCA$  which ranges from -4 ppb to -5 ppb. The SCA at these sites are variable but have a strong decreasing trend. ICE has a smaller  $\Delta SCA$  (-0.05) ppb compared the other three sites in the NHL. There is a large decrease in the SCA during the first 4 years of the study and then the SCA value steadily fluctuates between  $\sim 30$  and  $\sim 40$  ppb. This results in no trend in the SCA for the rest of the study period leading resulting in a smaller negative  $\Delta SCA$  compared to the other sites (See Supplement Fig. S2).

The Non-NHL regions had a mean observed  $\Delta SCA$  of 4 ppb. The three SHL sites sample well-mixed air and are less influenced by local sources. The concentrations at regional sites near to emissions are all affected in different ways, whereas at the sites in Antarctica the effect is smoothed out by the time air reaches the South Pole region. The 3 sites in Antarctica are

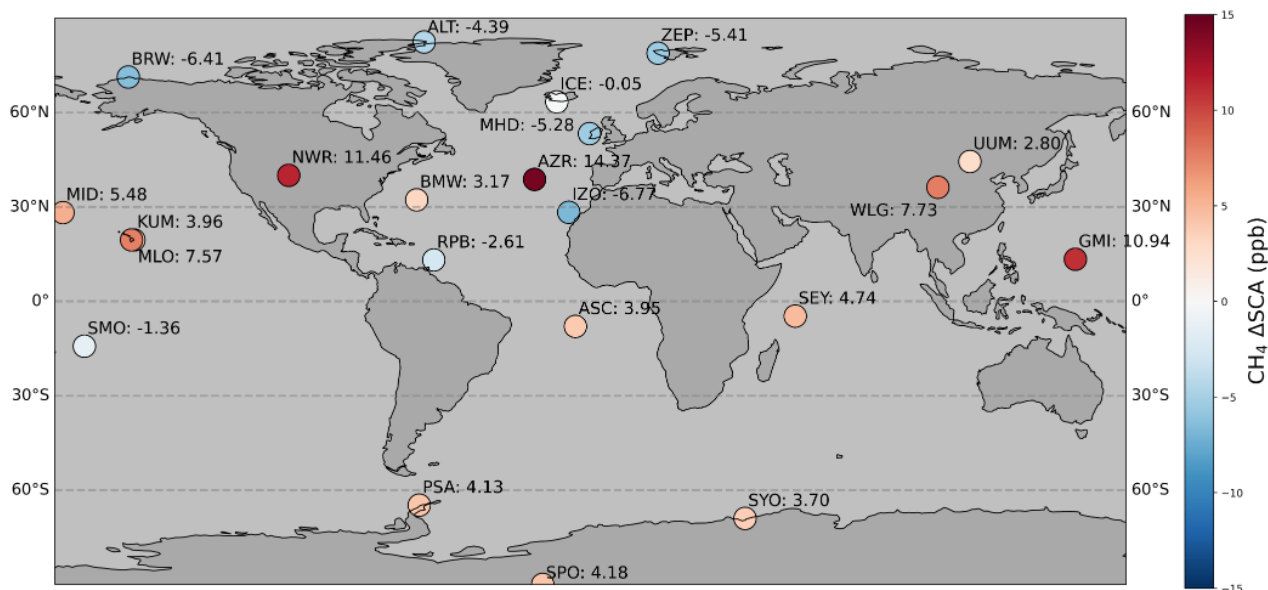


**Figure 3.** Map showing  $\Delta$ SCA (ppb) at the 22 selected observation sites.

exposed to well-mixed air and have the same mean increase of 4 ppb, highlighting that the observed  $\Delta$ SCA in NHL is very different to the global observed  $\Delta$ SCA. This implies that the Arctic is responding differently to the global increase in CH<sub>4</sub> concentrations than the rest of the world and therefore we focus on investigating the decreasing SCA in the NHL.

### 3.2 Model Evaluation

245 The observed CH<sub>4</sub> SCA is simulated well by TOMCAT with the surface fluxes from INVICAT in the TOM\_regional simulation (Fig. 4a). There is a strong linear relationship between the modelled and observed SCA with a mean bias of  $0.93 \pm 0.09$  ppb. However, the model struggles to capture the SCA at Mount Waliguan (WLG) in China. This is likely due to the fact that it has the highest altitude out of all the sites and the reasonably coarse model grid cell will not capture the local topography. The model simulation was also compared with sites that were not assimilated in INVICAT, although there are limited observations with

250 only 6 sites situated in the Northern Tropics and Northern Mid Latitudes. Due to these sites only having regular observations over a short time period, the comparison only covers the periods 1997-2015 and 2009-2015 (see Supplement). The model captures the SCA well at these independent sites, apart from Cape Ochi-ishi (COI) where the model has a weaker seasonal cycle, particularly during the seasonal cycle minimum. COI is situated near swamps, grazing lands and two cities, so it is possible that the model does not fully capture the complexity of the local sources well. There are large error bars ( $1\sigma$ ) for

255 the Siberian sites in both the modelled and observed SCA. This is due to the SCA being quite variable over the short time period available. However, the model still compares well with the observed SCA at these sites, with a mean overestimation of 16 ppb which is well within the  $1\sigma$  error. Full results of the independent analysis can be found in the Supplement, Fig. S1.

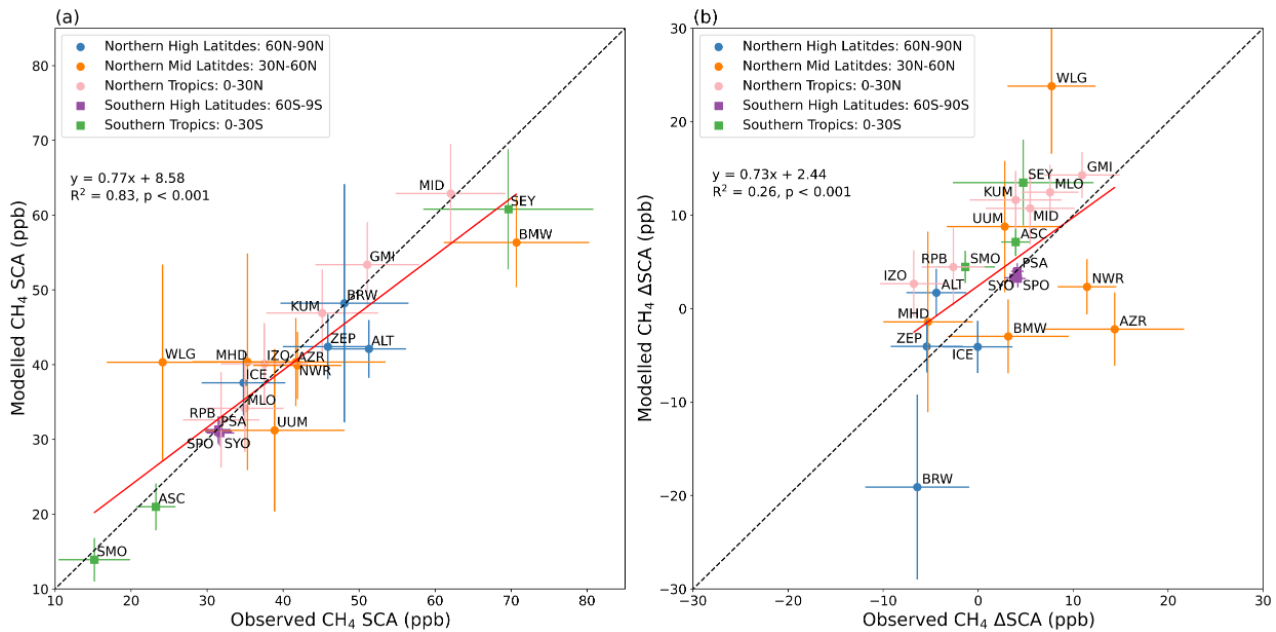


**Figure 4.** Comparison between simulated and observed (a)  $\text{CH}_4$  SCA (ppb) and (b)  $\text{CH}_4$   $\Delta$ SCA (ppb). The SCA shown is the mean SCA between 1995-2020 and  $\Delta$ SCA is the change in SCA for the same period. The dashed black line represents the 1:1 line and the red line represents the least squares regression line. The error bars denote  $\pm 1\sigma$ , which represents the interannual variability between 1995-2020.

The model captures the mean SCA when compared with NOAA observation sites well but there are larger differences with the independent sites, which is due, in part, to larger variability in the SCA over a shorter time period.

260 The model also captures  $\Delta$ SCA well when compared with observations, including the negative  $\Delta$ SCA and contrasting behaviour in the NHL shown by observations (Fig. 4b). As a result, we can use TOMCAT to inform us on what might be driving this significantly different behaviour in the NHL. There is a good correlation ( $r=0.51$ ) between the model and observations and they almost always match within the  $1\sigma$  uncertainty of observations, with some outliers. At ALT, TOMCAT shows a  $\Delta$ SCA of 1.7 ppb and this is due to TOMCAT underestimating the SCA when compared with observations, particularly at the beginning of the study period. At BRW the model has a much stronger negative  $\Delta$ SCA when compared with the observations and this is due to the model overestimating the SCA at the beginning of the study period. Despite the under- and over-estimations at these two sites (ALT and BRW) in the NHL, the mean value of  $\Delta$ SCA in TOMCAT is -6.38 ppb in the NHL, which shows a larger negative trend in the SCA than the observed mean  $\Delta$ SCA value of -4 ppb. This is mostly due to the This is mostly due to the overestimation of the magnitude of the simulated  $\Delta$ SCA at BRW. At WLG the model overestimates  $\Delta$ SCA, again this is likely  
 265  
 270 due to the model representation at this site. The time series of the SCA and its trend at each NOAA site can be found in the Supplement. The model performs better at the NOAA sites partly because these sites are used to provide optimised fluxes in our model and because  $\Delta$ SCA was calculated over a long time period of 25 years. The independent site at Mace Head (GC-MD) also performs because  $\Delta$ SCA is calculated over a period of 18 years. The independent sites in Siberia do not perform as well

compared to GC-MD and the NOAA sites because of the large variability in the SCA over the relatively short time period  
275 (6 years) of observations. Despite some differences between the model and observations in the NHL and Non-NHL regions,  
the model still captures the change in the SCA across the globe, almost all within  $1\sigma$  uncertainty of the observations. We are  
confident that the transport in the model is sufficient. Therefore, we can use TOMCAT to regionally attribute the changes in  
the SCA in the NHL.

### 3.3 The Role of OH

280 We use the TOM\_regional simulation to determine the influence the increasing abundance of  $\text{CH}_4$  in the atmosphere has on its  
removal by OH and the seasonal cycle. In the TOM\_regional simulation we use OH fields which vary month to month but do  
not vary from year to year due to uncertainty in the annual variability. Some studies find a declining trend in OH from 2004  
(Rigby et al., 2017; Turner et al., 2017) but Zhao et al. (2019) found an increasing trend in OH between 2000 and 2010. In  
contrast some studies only find small annual variability in OH (Patra et al., 2021; Naus et al., 2021). These studies contain large  
285 uncertainties and do not cover the full period of our study so a year to year variability in OH was not included our TOMCAT  
simulations.

We find, using TOMCAT, in the northern hemisphere the  $\Delta\text{SCA}$  due to OH loss is +1.0 ppb, and +1.1 ppb in the southern  
hemisphere. From this, we would expect the observation sites to show a  $\Delta\text{SCA}$  of  $\sim 1$  ppb in the absence of any other changes,  
and any deviations from that are due to changes in transport and/or emissions. These results inform our expectation that the  
290 SCA is expected to increase with the increasing atmospheric burden of  $\text{CH}_4$  due to more  $\text{CH}_4$  being removed by OH.

### 3.4 Regional Contribution to $\Delta\text{SCA}$ in Northern High Latitudes

We now assess what is driving the decreasing SCA in the NHL by analysing the regional contributions at NHL sites in the  
TOM\_regional simulation. Figure 5 shows the contribution of the background and tagged regions as a mean across all sites  
in each latitude band. The background tracer shows the largest contribution to negative  $\Delta\text{SCA}$  in the NHL (-9.93 ppb, Fig.  
295 5a). The background tracer represents  $\text{CH}_4$  that is well-mixed in the atmosphere, likely from emissions from distant regions.  
The largest regional contributors to the negative  $\Delta\text{SCA}$  in the NHL include Canada (-2.97 ppb), Middle East (-2.13 ppb) and  
Europe (-1.48 ppb), shown in Fig. 5b. The China & Japan region has the largest positive influence on NHL  $\Delta\text{SCA}$  (3.94 ppb).  
Despite some positive regional contributions of  $\Delta\text{SCA}$  to the NHL, the  $\Delta\text{SCA}$  in the NHL is still decreasing. This is due to  
the negative contribution of well-mixed emissions from the background tracer and large regional negative contributions from  
300 Canada, Europe and the Middle East.

The TOM\_transport simulation represents the contribution of transport to the negative  $\Delta\text{SCA}$  in the NHL and this simula-  
tion shows a different regional contribution compared to the TOM\_regional simulation (Fig. 5, TOM\_transport simulation is  
represented by the hatched bars). From this simulation we find that 33% of the negative  $\Delta\text{SCA}$  in the NHL is due to changes  
to transport and this can be split into contributions from the background and regional tracers. The largest contribution from  
305 transport as a fraction of the total contribution of the tracer is from the background tracer which accounts for 23% (-2.32  
ppb). Changes in the transport of emissions from North America and Russia have also contributed to the decrease in the SCA

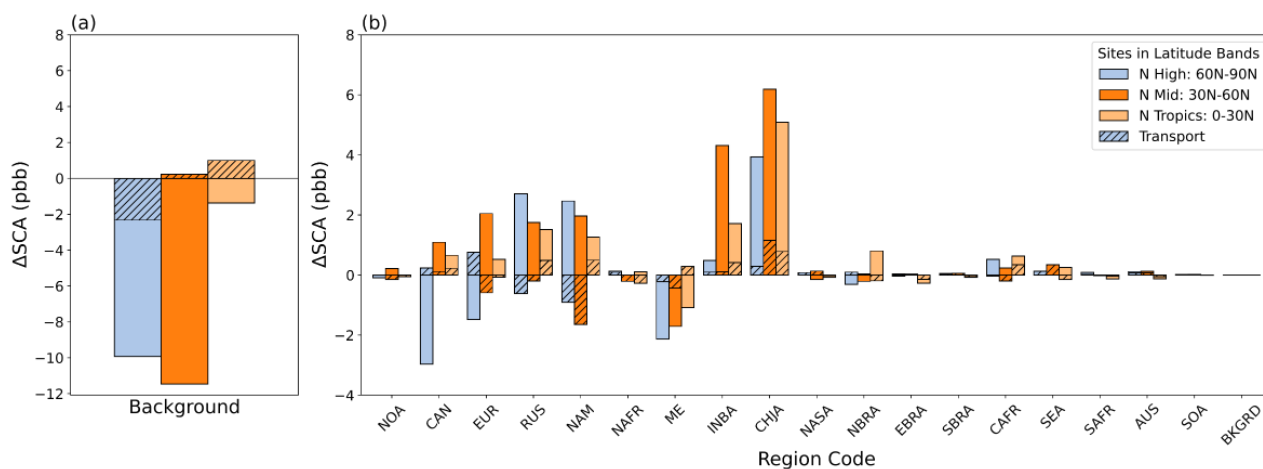


**Figure 5.** The contribution of the (a) background tracer and (b) regional tagged tracers to  $\text{CH}_4$   $\Delta SCA$  (ppb) for 1995-2020 as a mean across all sites in the latitude band. The blue bars show the NHL and the orange bars are the two Non-NHL latitude bands in the northern hemisphere. The hatched bars show the contribution from transport (TOM\_transport) and the solid colour represents the contribution from emissions (TOM\_regional). Note, (a) and (b) have different scales.

between 1995-2020 in the NHL, however the changes in emissions from these regions contribute to an increase in the SCA. The change in SCA due to emissions is larger in magnitude than the contribution from transport, resulting in overall increase in the SCA in the NHL from these regions. The TOM\_transport contribution to  $\Delta SCA$  in NHL from Canada and Europe is  
 310 0.24 ppb and 0.77 ppb, respectively, resulting in an increase in the SCA in the NHL due to changes in transport. However, changes in emissions result in an overall decrease in the SCA from these regions. This is due to the magnitude of the decrease in SCA being larger than the contribution from transport. This implies that their contributions to the negative  $\Delta SCA$  in NHL are due to changes in emissions. We also assess the effect the size of the regional tracers has on our results by normalising the regional contribution by area size. We find the largest contributors to the decreasing SCA in the NHL are still due to changes  
 315 in emissions from Canada, Middle East and Europe (see Supplement Fig. S3).

The TOMCAT simulations (TOM\_regional and TOM\_transport) show the largest contributions to the decrease in  $\Delta SCA$  in the NHL are mostly due to changes in emissions from Canada, Middle East and Europe. To further investigate the changes in emissions that are driving the negative  $\Delta SCA$  in the NHL we look at the trends of the regional  $\text{CH}_4$  concentration (ppb) contributions from the TOM\_regional and TOM\_transport simulation as a mean across all sites in the NHL. We refer to these  
 320 regional  $\text{CH}_4$  concentration contributions as the tracer contribution. We also assess the trends of the seasonal emissions from each region. Often the trends in both the  $\text{CH}_4$  contributions and the regional emissions are not statistically significant due to their large variability over time. However, we are interested in the direction of these trends in order to determine how emissions and transport from each region are changing over time and their impact on the seasonal cycle in the NHL. We compare the seasonal trends of regional tracer contributions (ppb) to the NHL from the TOMCAT\_regional and TOMCAT\_transport  
 325 to further assess the contribution of emissions and transport from individual tracers. If the trend in the TOMCAT\_transport

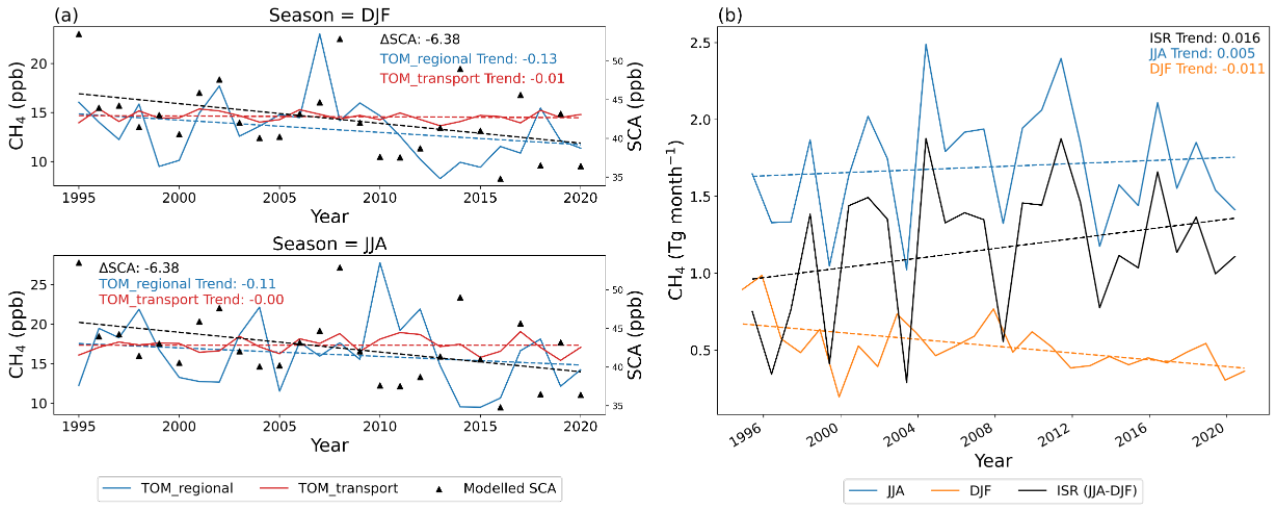


**Figure 6.** (a) Canada's seasonal mean CH<sub>4</sub> (ppb) contribution to the NHL sites (60N-90N) for TOM\_regional (blue) and the TOM-CAT\_transport simulation (red) for 1995-2020. (b) Canada's seasonal mean emissions (Tg month<sup>-1</sup>) from the inversion for JJA (blue), DJF (orange) and the interseasonal range (ISR, black) for 1995-2020.

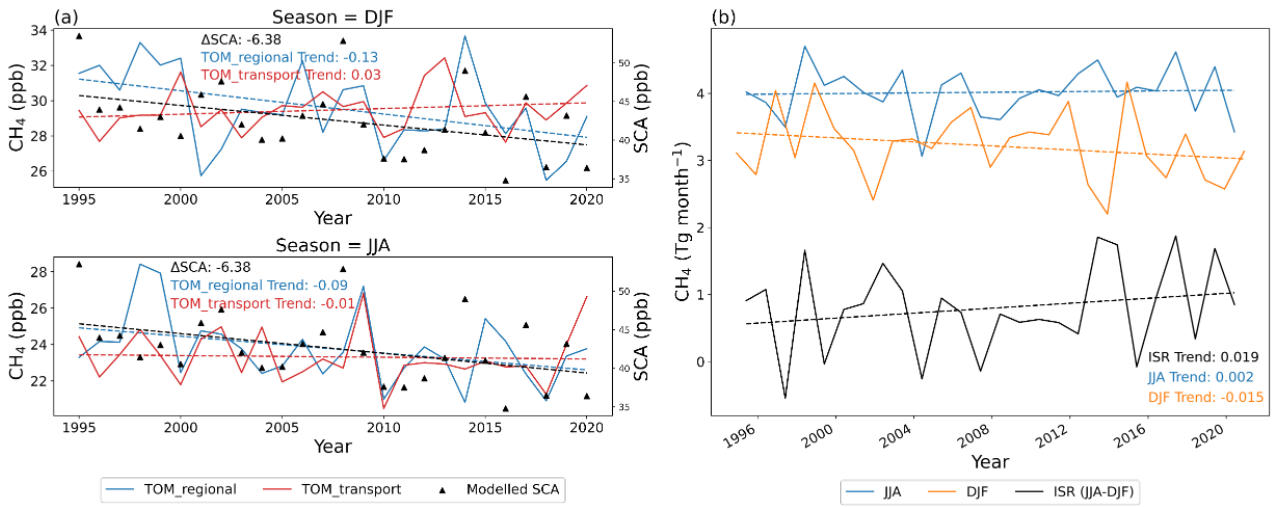


**Figure 7.** (a) Europe's mean CH<sub>4</sub> (ppb) contribution to the NHL sites (60N-90N) for the TOMCAT\_regional (blue) and the TOM-CAT\_transport simulation (red) for 1995-2020. (b) Europe's mean emissions (Tg month<sup>-1</sup>) from the inversion for JJA (blue), DJF (orange) and the interseasonal range (ISR, black) for 1995-2020.

simulation is comparable to the trend in the TOMCAT\_regional simulation we can attribute the change to transport and not emissions. To assess the change in the seasonal emissions we calculated the inter-seasonal range (ISR, Tg month<sup>-1</sup>) which represents the difference between June, July, August (JJA) and December, January, February (DJF) seasonal mean emissions. It

is important to note that the emission seasonal cycle is out of phase with the concentration seasonal cycle at northern mid- and high latitudes, so a positive ISR in emissions leads to a decreasing SCA. This is because the CH<sub>4</sub> seasonal cycle minimum is during the summertime in the NHL, so increasing emissions during this time would raise the minimum value, thereby shrinking the seasonal cycle. Similarly, shrinking wintertime emissions would bring down the seasonal maximum which occurs at the same time. This effect is mostly likely in regions near to sites in the NHL. We focus on the three largest regional contributors to the negative  $\Delta$ SCA in the NHL: Canada, Europe and the Middle East. We also focus on the largest regional positive contributor of  $\Delta$ SCA in the NHL, China & Japan, to assess its impact on the decreasing SCA at NHL sites.

When we look at the regional tracer contributions in the NHL from Canada and Europe we find stronger trends in the TOM<sub>regional</sub> simulation, compared with no trends shown in the TOM<sub>transport</sub> simulation during DJF and JJA seasons (Fig. 6a) and Fig. 7a). This shows that changes in emissions in these regions are driving the decrease in the NHL. This is also shown by a positive ISR in emissions from Canada and Europe (Fig. 6b and Fig. 7b). The Middle East's tracer contribution in the NHL shows no trends in the TOM<sub>transport</sub> simulation which means that changes in transport from this region has very little impact on the SCA in the NHL (Fig. 8a). As a result, changes in emissions in the Middle East are the mostly driving the decrease in the SCA in the NHL. This is also shown by a positive ISR in emissions from the Middle East (Fig. 8b). Changes in emissions are the main contributor to the decrease in the SCA in the NHL from Canada, the Middle East and Europe. China & Japan contributes the most to increasing the SCA in the NHL, however the overall changes in emissions and transport from the background tracer and other regions still results in a decreasing SCA. We find that a combination of changes in emissions and changes in transport from China & Japan are causing an increase in the SCA in the NHL from this region (Fig. 9). By comparing the TOM<sub>regional</sub> and TOM<sub>transport</sub> simulations and the seasonal changes in emissions in these regions, we find that changes in emissions are the largest driver in changes in the SCA in the NHL.

Changes in emissions from Canada are mostly driven by increasing JJA emissions and decreasing DJF emissions. The changes in seasonal emissions lead to a positive ISR ( $0.02 \text{ Tg month}^{-1} \text{ year}^{-1}$ ,  $p\text{value}=0.17$ , Fig. 6b). The trend of the DJF tracer contribution in the TOM<sub>regional</sub> is decreasing at a faster rate ( $-0.13 \text{ ppb month}^{-1}$ ,  $p\text{value} = 0.13$ ) than the JJA ( $-0.11 \text{ ppb month}^{-1}$ ,  $p\text{value} = 0.36$ ), which results in a decrease in the SCA. There is some uncertainty in the trends of both the emissions and tracer contributions due to their large variability during the study period. The combination of weak trends in TOM<sub>transport</sub> simulation and the positive ISR indicates that changes in DJF and JJA emissions from Canada is the main contributor to the decreasing SCA in this region.

The emissions from Europe during JJA are increasing slightly but there is a stronger decrease in the DJF emissions. The decrease in winter emissions result in a positive ISR ( $0.02 \text{ Tg month}^{-1} \text{ year}^{-1}$ ,  $p\text{value}=0.3$ , Fig. 7b). The mean CH<sub>4</sub> tracer contribution from Europe to the NHL sites in the TOM<sub>transport</sub> simulation shows a small positive trend in DJF and a very small decreasing trend in JJA (Fig. 7a). This shows that changes in winter transport are contributing to an increase in the SCA in the NHL. However large variability in the TOM<sub>transport</sub> concentrations leads to some uncertainty on how much transport is having an impact from this region. The changes in emissions in the TOM<sub>regional</sub> simulation contribute more to a decrease in the SCA. The TOM<sub>regional</sub> DJF tracer contributions ( $-0.13 \text{ ppb month}^{-1}$ ,  $p\text{value}=0.02$ ) from Europe are decreasing at a faster rate than the JJA tracer contributions ( $-0.09 \text{ ppb month}^{-1}$ ,  $p\text{value}=0.06$ ), resulting in an decrease in the SCA. The positive

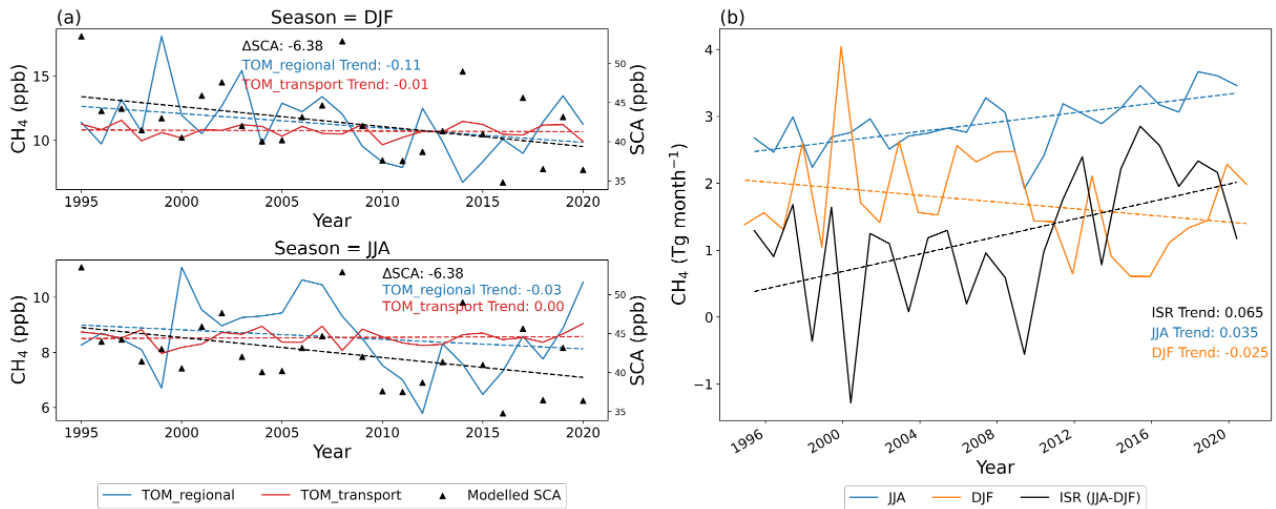


**Figure 8.** (a) The Middle East’s mean CH<sub>4</sub> (ppb) contribution to the NHL sites (60N-90N) for the TOM\_regional simulation (blue) and the TOM\_transport simulation (red) for 1995-2020. (b) The Middle East’s mean emissions (Tg month<sup>-1</sup>) from the inversion for JJA (blue), DJF (orange) and the interseasonal range (ISR, black) for 1995-2020.

ISR is supported by trends in the tracer contributions being statistically significant which shows that changes in emissions from this region are driving the decrease in NHL.

The emissions from the Middle East are increasing in JJA and decreasing in DJF, which results in a positive ISR (0.07 Tg month<sup>-1</sup> year<sup>-1</sup>, pvalue=0.01, Fig. 8b). The mean CH<sub>4</sub> tracer contribution from the Middle East to the NHL sites is decreasing in both JJA (-0.04 ppb month<sup>-1</sup>, pvalue=0.3) and DJF (-0.11 ppb month<sup>-1</sup>, pvalue=0.07) in the TOM\_regional simulation (Fig. 8a). The trend in DJF is decreasing faster than the trend in JJA, resulting in a decrease in the SCA. The combination of the positive trend in the ISR being statistically significant and the fast decreasing winter concentrations indicates that changes in emissions from this region are the main contributor to the decrease in the SCA in the NHL.

The emissions from China & Japan are decreasing slightly in JJA and increasing in DJF, resulting in a negative ISR (-0.07 Tg month<sup>-1</sup> year<sup>-1</sup>, pvalue=0.05, Fig. 9b). The mean CH<sub>4</sub> tracer contribution from this region to the NHL is increasing in DJF and JJA in the TOM\_regional simulation (Fig. 9a). The DJF contribution is increasing at a faster rate (0.15 ppb month<sup>-1</sup>, pvalue=0.03) than the JJA contribution (0.07 ppb month<sup>-1</sup>, pvalue=0.21), resulting in an increase in the SCA. The TOM\_transport simulation shows a small trend in DJF (0.015 ppb month<sup>-1</sup>, pvalue=0.32) in the tracer contribution from this region and no trend in the JJA contribution, showing that transport is also contributing to an increase in the SCA in NHL. However there is some uncertainty in how much transport is having an impact due to the large variability in the trends in tracer contribution in the TOM\_transport simulation. The TOMCAT simulations and emission trends show that changes in emissions and DJF transport from China & Japan contributes to an increase in the SCA in the NHL. However, the overall contribution from the background tracer and other regional tracers still results in a decrease in the SCA in the NHL.



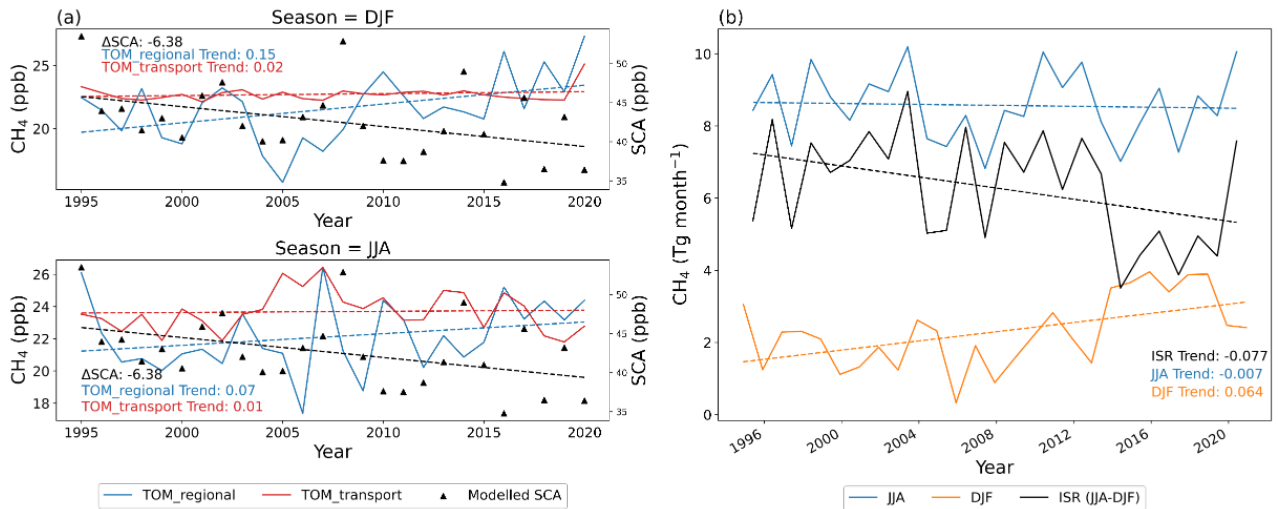


**Figure 9.** (a) shows China & Japan’s mean CH<sub>4</sub> (ppb) contribution to the NHL sites (60N-90N) for the TOMCAT\_regional (blue) and the TOMCAT\_transport simulation (red) for 1995-2020. (b) shows China & Japan’s mean emissions (Tg month<sup>-1</sup>) from the inversion for JJA (blue), DJF (orange) and the interseasonal range (ISR, black) for 1995-2020.

### 3.5 Sensitivity Experiments

We carried out two sensitivity experiments to examine the impact of shorter and longer decay rates of regional tracers into the background tracer. These simulations are described in Sect. 2.2. The TOM\_twelve simulation showed that changing the exponential decay rate from 9 months to 12 months did not change the largest contributors to the ΔSCA. This implies that after 9 months, CH<sub>4</sub> emissions has undergone long-range transport and no longer has a distinguishable emission origin, so has become well-mixed. Reducing the exponential decay rate to 1 month did, however, have an impact on the final results. The TOM\_one simulation showed larger regional contributions in the NHL from Canada than the background tracer. The contribution from the background tracer in the TOM\_one simulation contains emissions from southern regions because emissions from these regions will have been moved into the background tracer before they had the chance to reach the NHL. For regions close to the NHL sites, such as Canada and Russia, we can see the effect of those emissions before they become well-mixed. The recent local emissions from Canada are having an impact on the decreasing SCA but the effects of mixing and changes in transport will reduce this impact. These sensitivity experiments show that the 9-month decay rate into the background is a good compromise for quantifying well-mixed emissions. It allows us to look at the effect from relatively recent emissions and also allows enough time for far-away emissions to be transported to the NHL in order to quantify their effect on the ΔSCA. More details on the sensitivity study can be found in Appendix A.

## 4 Discussion

Using the NOAA surface observations we have shown that globally the SCA of CH<sub>4</sub> is increasing but in the NHL it is decreasing. As the atmospheric burden of CH<sub>4</sub> is increasing it would be expected that the SCA would show a corresponding increase due to greater removal of CH<sub>4</sub> by OH in the atmosphere. Therefore, the change in the SCA in the NHL is counter-intuitive and we explore through TOMCAT simulations what is driving this decreasing SCA. A persistent change in the SCA indicates a long-term change in the sources, sinks and/or transport of CH<sub>4</sub> and the decreasing SCA in the NHL indicates a different response to the increasing atmospheric CH<sub>4</sub> burden compared to the rest of the world.

We use a TOMCAT-based atmospheric inversion which assimilates NOAA surface observations across the globe. There is a much greater number of sites situated in the northern hemisphere, compared with the southern hemisphere. There are large and variable sources of CH<sub>4</sub> in central Africa and Brazil but the model is not well constrained over these regions due to the lack of observations. The large contribution of emissions to the global CH<sub>4</sub> budget from central Africa and Brazil has been highlighted in a number of recent studies (Lunt et al., 2021; Wilson et al., 2021; Feng et al., 2022) so the surface emissions in our study might not fully capture the magnitude and distribution of emissions from these regions due to the lack of observations.

The TOMCAT tagged tracer simulations perform well when compared with observations (Fig. 4). However, from Fig. 4b it is noted that BRW, which is situated in the NHL, is an outlier in the model, compared with other sites. The model does capture the change in the SCA within the observation uncertainties, but these are large for this site. To test the influence of BRW on our results we removed it from our analysis. We find that Canada is no longer the largest regional contributor to the decrease in the SCA in the NHL and, in fact, contributes to an increase in the SCA at the other sites (ALT, ICE & ZEP). However, Europe and the Middle East remain the largest contributors to the decrease in the SCA at ALT, ICE and ZEP (See Supplement Fig. S4). The removal of BRW from our analysis shows that local emissions are having the largest impact at this site. This is likely due to a strong decrease in emissions in DJF and an increase in emissions in JJA in Alaska and western Canada during the study period (See Supplement Fig. S6b). The seasonal changes in emissions over eastern Canada are different to Alaska and western Canada and it is likely that a different mechanism is having an effect on the other sites in the NHL. This test shows that the boundaries of the tagged tracer regions and the proximity of Canada and Europe to the NHL does have an impact on the results. For example, if Alaska was grouped into the North America (NAM) region, then NAM could be a large contributor to the decrease in the SCA due to the changes in emissions over Alaska. However, we include Alaska and Canada as one region due to their similar biomes and meteorology. Despite some differences between the model and observations (e.g. at ALT and BRW), TOMCAT does capture the significantly different behaviour in the NHL compared to the rest of the globe. The change in SCA in the NHL is consistently lower compared to the rest of the globe, implying that increasing emissions, both local and non-local, are impacting the NHL differently.

The main focus of our analysis was in the NHL, however observations Mace Head (MHD) also show a decreasing SCA, similar to what is observed in the NHL. When we included MHD in our analysis by extending the NHL (NHL\_ext, 52N-60N), we found that its proximity to emission regions had an effect on the regional contribution to  $\Delta$ SCA in the NHL\_ext. Changes in emissions from Canada and the Middle East, and changes in transport from North America and the Middle East contribute

the most to the decrease in the NHL\_ext SCA. Europe contributes to an increase in the SCA in the NHL\_ext (see Supplement Fig S5). This is because MHD is strongly influenced by local trends in emissions in western Europe (see Supplement Fig. 8b). The seasonal changes in eastern Europe are quite different to western Europe, which are likely to affect the sites north of 60N differently to MHD.

435 We can use the model to regionally attribute the change in the SCA because it performs well when compared with observations. However, it is difficult to disaggregate the contribution of different emission types within these regions. When possible, we have estimated emission types by looking at emission maps of each of the largest regional contributors and referring to literature. In addition to regional contributions, the regional tracers were allocated to a background tracer using an exponential 9-month decay rate to represent well-mixed methane that no longer has a distinguishable emission origin. It is not possible to  
440 tell from our simulations what regions are contributing the most to the background tracer.

We have shown through TOMCAT simulations that well-mixed (background) CH<sub>4</sub>, likely from emissions from regions far from the NHL, along with regions in the lower northern latitudes, are having a large influence on the SCA in the NHL. Whilst transport from the background tracer is a contributing factor to the decrease in the SCA in the NHL, 83% of all tracer contributions are due to emissions. Here we discuss the emissions sectors that might be driving these seasonal changes from  
445 the largest regional contributors to the change in the SCA in NHL. These include Canada, Europe, Middle East and China & Japan.

Canada has the largest negative contribution to the  $\Delta$ SCA NHL due to emissions (-2.97 ppb), however we have shown that this region predominantly affects BRW. An increase in JJA and a decrease in DJF emissions have impacted the CH<sub>4</sub> contribution in the NHL, leading to a decrease in the SCA. There are a number of different sources which could contribute  
450 to the changes in emissions in Canada. Anthropogenic sources of CH<sub>4</sub> in Canada include oil and gas, livestock and landfills and natural sources include wetlands and biomass burning (Scarpelli et al., 2021). Studies investigating the seasonality of the Hudson Bay Lowlands, the second largest boreal wetland in the world, found the wetland emissions peak in July/August and decreases significantly in September-to-November (Pickett-Heaps et al., 2011; Fujita et al., 2018). Fujita et al. (2018) also found that biogenic sources are the most dominant for the seasonal cycle in this region and that the boreal wetlands are the  
455 main source. They found that fossil fuels and biomass burning are minor contributors to the CH<sub>4</sub> concentration seasonal cycle. Fossil fuels are often classed as a nonseasonal source but Fujita et al. (2018) find that they contribute significantly to the mole fraction of CH<sub>4</sub> in early winter at the Churchill observation site situated on Hudson Bay's coast. This implies that fossil fuel emissions have some seasonality in this region, peaking in winter. Lu et al. (2021) report that top-down estimates from satellite data show a decreasing trend in anthropogenic emissions for 2010-2017. The emissions used in our model show a decrease  
460 annually in September, indicating the wetlands are a large factor in this region's season cycle. The mean seasonal emissions for the study period peak in JJA over western Canada which is an area prone to wildfires and emissions are also large around the Boreal Plains (Environment and Climate Change Canada, 2016). Also the GFED fire emissions database (van der Werf et al., 2017) shows that annual emissions of CH<sub>4</sub> from biomass burning have been increasing from 1997-2020 (0.03 Tg year<sup>-1</sup>, pvalue=0.01, see Supplement Fig. S10). Despite the emission trends in our results having high p-values, the direction of the  
465 trends follow changes reported by literature. It is likely that wetland and biomass burning emissions are increasing during the

summer in Canada, contributing to the negative  $\Delta$ SCA contribution to the NHL, predominantly at BRW, with some influence of decreasing anthropogenic emissions in the winter. The positive trends in emissions are often over wetland and biomass burning regions during summer and the winter decrease in emissions is strongest in western Canada where there are a few main cities (See Supplement, Fig. S6b).

470 The Middle East region has the second largest contribution to the decreasing SCA in the NHL (-2.13 ppb). The trend in the ISR of emissions from the Middle East has a pvalue of 0.01 which further implies that emissions are responsible for the contribution to the negative  $\Delta$ SCA in NHL. Emissions in this region are dominated by anthropogenic emissions such as oil and gas, agriculture and waste. A recent study has shown that the Middle East is one of the largest contributors to the rise in  $\text{CH}_4$  emissions between 2000 and 2017 (Stavert et al., 2022). Our emission maps show the largest emissions in JJA, particularly  
475 over the Caspian Sea and the Persian Gulf, which is a region of significant oil and gas extraction. The seasonality of emissions from this region is not well documented so it is not possible to be certain of the change in emissions in this region that is contributing to the decreasing SCA in the NHL. The emissions used in the model indicate the largest increases in emissions in JJA and decreases in DJF emissions are in areas known for oil and gas extraction (Supplement, Fig. S7b). From this, it is likely that anthropogenic emissions are driving the changes in contribution to the decrease in SCA in the NHL from this region.

480 Europe is the third largest contributor to the decrease in the SCA in the NHL (-1.48 ppb). The TOM\_regional JJA and DJF trends in the concentration contributions to the NHL from this region are  $0.06 \text{ ppb year}^{-1}$  and  $0.02 \text{ ppb year}^{-1}$ , respectively. This highlights that it is mostly emissions contributing to the decrease in the SCA in this region. Emissions in Europe include natural sources such as wetlands, peatlands and wet soils, and anthropogenic emissions such as agriculture, waste and fossil fuels (Bergamaschi et al., 2018). It is often assumed that wetlands have the strongest seasonality and Bergamaschi et al.  
485 (2018) explained that precipitation is important for southern European wetlands but temperate and boreal wetlands are driven by temperature variations. Southern European wetlands could be impacted by a decreasing trend in precipitation shown by Christidis and Stott (2022), which could result in a decrease in wetland emissions. It is hard to say what emission types are driving the decrease in winter emissions over Europe due to lack of studies of the seasonality of sources in this region; it is possible that sources other than wetlands are having an impact. For example, improvements in the efficiency of fossil fuel use,  
490 domestic and/or extraction could result in lower  $\text{CH}_4$  emissions in winter.

China & Japan is the region which contributes the most to an increase in the SCA in the NHL. The DJF concentration contribution has a p-value of 0.02 so it is likely that this season is driving this positive contribution. Emissions in China & Japan are mostly driven by agriculture and waste and fossil fuels (Stavert et al., 2022). Stavert et al. (2022) found that fossil fuel emissions have increased by 114% in bottom-up estimates and 78% in top-down estimates between 2000 and 2017.  
495 The differences arise due to the emission inventories diverging towards the end of their study period. However, this does show that fossil emissions from China have increased significantly over the last two decades. Approximately 40% of China's anthropogenic emissions are from fossil fuels and the remainder is split equally between livestock, rice paddies and waste (Stavert et al., 2022). Our emissions show the largest emissions are situated in south east China (Supplement, Fig. S9) where rice paddies, oil and gas, and waste are the main sources of  $\text{CH}_4$  (Peng et al., 2016). Despite the fact that emissions are generally  
500 increasing in China and causing a large positive contribution to  $\Delta$ SCA in the NHL, the SCA in the NHL is still decreasing.

We find that Russia does not contribute to the decrease in the SCA in the NHL, despite it being a region that has large natural and anthropogenic emissions of CH<sub>4</sub>. The Russian emissions used in the forward simulation are not locally constrained before 2011 but transport from Russia to the NHL sites is short (~2 weeks) because it is largely zonal (Jacob, 1999). The inversion and forward simulations represent transport of emissions well which means that the four sites in NHL will be impacted by Russian emissions throughout the study period, even when the inversion has few sites to constrain the model in this region. Our results show that changes in transport from Russia contribute to a small decrease in the SCA with a  $\Delta$ SCA of -0.6 ppb (See Fig. 5b). This is a small contribution to the decrease in the SCA in the NHL, which is why we decided to focus on Canada, the Middle East and Europe as they have the largest contributions to decrease in the SCA in the NHL.

There is some uncertainty in the seasonality of CH<sub>4</sub> emissions and how they change over time in Canada, the Middle East, Europe and China & Japan. The emissions used in TOMCAT were discussed in Section 2.3. Our inversion uses prior information from various emission inventories. The prior emissions that predominantly drive the seasonal cycle are wetland emissions from WetCHARTS model and biomass burning emissions from GFEDv4.1s. These emission estimates have been evaluated in previous CH<sub>4</sub> studies (e.g. Parker et al. (2020) and Liu et al. (2020)). These prior emissions are optimised, including their seasonality, when the surface observations are assimilated in our inversion. This means that our emissions used in TOMCAT are optimised seasonally, however it is difficult to disaggregate the emission sectors driving the total emissions' seasonal cycle in each region.

The three main regions that contribute the most to the decreasing SCA in the NHL (Canada, Europe and Middle East) have common trends in emissions and tracer contributions to the NHL sites. The trends in regional tracer contributions across the whole of the NHL at the surface show similar results (See Supplement). In each region the winter emissions are generally decreasing and summer emissions are increasing over the study period. Similarly the regional DJF tracer contribution to the NHL generally decreases at a faster rate than the JJA tracer contribution, resulting in a decrease in the SCA, despite the fact that emissions from the region are increasing in JJA. This is likely due to a redistribution of emissions over time from each region, causing it to be transported differently to the NHL. We have shown that changes in well-mixed emissions and changes in emissions from Canada, Europe and the Middle East are the main contributors to the decreasing SCA in the NHL. The results show that the CH<sub>4</sub> SCA is changing and this should act as motivation to investigate the seasonality of emissions as it highlights changes in the CH<sub>4</sub> budget.

## 5 Conclusions

We have used a 3-D chemical transport model, TOMCAT, with emissions derived from surface observations, to investigate changes in the SCA of CH<sub>4</sub>. Using TOMCAT we find that the global mean SCA increased by 1 ppb between 1995-2020 due to the increase in atmospheric CH<sub>4</sub> but this is offset by changes in emissions and transport. The NOAA surface observations show that globally the SCA has increased by a mean value of 2.5 ppb (6.5%) but decreased by 4 ppb (7.6%) in the NHL. The decreasing SCA in the NHL therefore does not follow the global trend and indicates that the seasonal cycle is responding differently to the global increase in atmospheric CH<sub>4</sub>.

Our study focused on what was driving the decrease in the SCA in the NHLs and found that well-mixed methane, allocated  
535 to a modelled background tracer, was the largest contributor. Around 33% of the background tracer's contribution to the NHL  
could be attributed to changes in transport whilst the remaining contribution is from emissions. The background tracer contains  
CH<sub>4</sub> that has become well-mixed and no longer has a distinguishable emission origin. Emissions from distant regions are  
likely to be main contributors to the background tracer as it is transported to the NHL. The largest regional contributions to the  
negative  $\Delta$ SCA in the NHL are from Canada, Europe and the Middle East. Increases in summer emissions from the Boreal  
540 Plains in Canada, decreases in winter emissions across Europe, and a combination of increases in summer emissions and  
decreases winter in emissions over the Arabian Peninsula and Caspian Sea in the Middle East are the other main contributors  
to the decrease in the SCA in the NHL.

The lack of studies that investigate the seasonality of emissions makes it hard to determine the source sector that is driving  
the change in emissions in these regions. The changes in the SCA in the NHL and globally indicate a long-term change in  
545 sources of CH<sub>4</sub> and highlight the seasonal response to the increasing CH<sub>4</sub> burden. More work is needed to investigate the  
seasonality of the sources that are having an impact on the decreasing SCA in the NHL.

*Code and data availability.* The NOAA data (Dlugokencky et al., 2021) are available from <https://doi.org/10.15138/VNCZ-M766> (last access: 2nd December 2021). The AGAGE data (Prinn et al., 2018) are available from <https://doi.org/10.3334/CDIAC/atg.db1001> (last access: 26th May 2022). The observations for Cape Ochi-ishi can be found at <https://doi.org/10.17595/20160901.004> and Hateruma Island can be  
550 found at <https://doi.org/10.17595/20160901.003> (last access: 8th November 2021). The Siberian tower observations are available through  
registration at the Global Environmental Database <https://db.cger.nies.go.jp/ged/en/> (last accessed: 19th October 2022). The GFED fire emis-  
sions (van der Werf et al., 2017) can be found at <https://www.globalfiredata.org/>. The TOMCAT detrended time series at the 22 observation  
sites are available at <https://doi.org/10.5281/zenodo.7997653>. Readers should contact the lead author to enquire about the use of the TOM-  
CAT model.

## 555 **Appendix A: Sensitivity Testing on Background Tracer**

We carried out a sensitivity experiment on the exponential decay of the CH<sub>4</sub> tracer into the background. The results of these  
model runs showed that changing the e-folding time (lifetime) from 9 months to 12 months did not have a large impact on the  
results. We also set the lifetime to 1 month, this did have an impact on the final results but 1 month lifetime is too short to  
represent well-mixed methane. Find the results of the model simulations in Table A1.

560 *Author contributions.* ED, CW, EG and MPC designed the study, ED carried out forward model simulations, inversions were carried about  
by CW, both with input from MPC. AM and RD provided guidance for data analysis. All co-authors contributed to the writing and analysis  
of the results.

*Competing interests.* The authors declare that they have no conflict of interest.

*Acknowledgements.* This work was supported by the Natural Environment Research Council (NERC) SENSE CDT studentship (NE/T00939X/1).

565 This work was also supported by NERC grants NE/V006924/1 and NE/V011863/1. We would like to thank NOAA GML CCGG for providing  
the long term, global surface observations. We would also like to thank M. Sasakawa and Y. Tohjima at the Center for Global Environmental  
Research Earth System Division National Institute for Environmental Studies for providing the independent observations in Siberia and at  
Haterma and Ochi-ishi. The station at Mace Head (GC-MD) is supported by the UK Department of Business Energy and Industrial Strat-  
egy(BEIS) (Contract number:TRN1537/06/2018). The operation and calibration of the global AGAGE measurement network are supported  
570 by NASA's Upper Atmosphere Research Program through grants NAG5-12669, NNX07AE89G, NNX11AF17G, and NNX16AC98G (to  
MIT) and NNX07AE87G, NNX07AF09G, NNX11AF15G, and NNX11AF16G (to SIO).

## References

- Basso, L. S., Marani, L., Gatti, L. V., Miller, J. B., Gloor, M., Melack, J., Cassol, H. L. G., Tejada, G., Domingues, L. G., Arai, E., Sanchez, A. H., Corrêa, S. M., Anderson, L., Aragão, L. E. O. C., Correia, C. S. C., Crispim, S. P., and Neves, R. A. L.: Amazon methane budget derived from multi-year airborne observations highlights regional variations in emissions, *Communications Earth & Environment*, 2, <https://doi.org/10.1038/s43247-021-00314-4>, 2021.
- Bergamaschi, P., Karstens, U., Manning, A. J., Saunio, M., Tsuruta, A., Berchet, A., Vermeulen, A. T., Arnold, T., Janssens-Maenhout, G., Hammer, S., Levin, I., Schmidt, M., Ramonet, M., Lopez, M., Lavric, J., Aalto, T., Chen, H., Feist, D. G., Gerbig, C., Haszpra, L., Hermansen, O., Manca, G., Moncrieff, J., Meinhardt, F., Necki, J., Galkowski, M., O'Doherty, S., Paramonova, N., Scheeren, H. A., Steinbacher, M., and Dlugokencky, E.: Inverse modelling of European CH<sub>4</sub> emissions during 2006–2012 using different inverse models and reassessed atmospheric observations, *Atmospheric Chemistry and Physics*, 18, 901–920, <https://doi.org/10.5194/acp-18-901-2018>, 2018.
- Bloom, A. A., Bowman, K. W., Lee, M., Turner, A. J., Schroeder, R., Worden, J. R., Weidner, R., McDonald, K. C., and Jacob, D. J.: A global wetland methane emissions and uncertainty dataset for atmospheric chemical transport models (WetCHARTs version 1.0), *Geoscientific Model Development*, 10, 2141–2156, <https://doi.org/10.5194/gmd-10-2141-2017>, 2017.
- Chipperfield, M. P.: New version of the TOMCAT/SLIMCAT off-line chemical transport model: Intercomparison of stratospheric tracer experiments, *Quarterly Journal of the Royal Meteorological Society*, 132, 1179–1203, <https://doi.org/https://doi.org/10.1256/qj.05.51.2006>.
- Christidis, N. and Stott, P. A.: Human Influence on Seasonal Precipitation in Europe, *Journal of Climate*, 35, 5215–5231, <https://doi.org/10.1175/JCLI-D-21-0637.1>, 2022.
- Crippa, M., Guizzardi, D., Muntean, M., and E, S.: EDGAR v5.0 Global Air Pollutant Emissions, <http://data.europa.eu/89h/377801af-b094-4943-8fdc-f79a7c0c2d19>, 2021.
- Dlugokencky, E., Crotwell, A., Mund, J., Crotwell, M., and Thoning, K.: Atmospheric Methane Dry Air Mole Fractions from the NOAA GML Carbon Cycle Cooperative Global Air Sampling Network, 1983-2020, Version: 2021-07-30, <https://doi.org/10.15138/VNCZ-M766>, 2021.
- Dlugokencky, E. J., Steele, L. P., Lang, P. M., and Masarie, K. A.: The growth rate and distribution of atmospheric methane, *Journal of Geophysical Research: Atmospheres*, 99, 17 021–17 043, <https://doi.org/https://doi.org/10.1029/94JD01245>, 1994.
- Dlugokencky, E. J., Masarie, K. A., Tans, P. P., Conway, T. J., and Xiong, X.: Is the amplitude of the methane seasonal cycle changing?, *Atmospheric Environment*, 31, 21–26, [https://doi.org/10.1016/S1352-2310\(96\)00174-4](https://doi.org/10.1016/S1352-2310(96)00174-4), 1997.
- Environment and Climate Change Canada: Canadian Environmental Sustainability Indicators: Extent of Canada's Wetlands, accessed 25/10/2022, 2016.
- Etiopie, G., Ciotoli, G., Schwietzke, S., and Schoell, M.: Gridded maps of geological methane emissions and their isotopic signature, *Earth System Science Data*, 11, <https://doi.org/10.5194/essd-11-1-2019>, 2019.
- Feng, L., Palmer, P. I., Zhu, S., Parker, R. J., and Liu, Y.: Tropical methane emissions explain large fraction of recent changes in global atmospheric methane growth rate, *Nature Communications*, 13, <https://doi.org/10.1038/s41467-022-28989-z>, 2022.
- Fujita, R., Morimoto, S., Umezawa, T., Ishijima, K., Patra, P. K., Worthy, D. E. J., Goto, D., Aoki, S., and Nakazawa, T.: Temporal Variations of the Mole Fraction, Carbon, and Hydrogen Isotope Ratios of Atmospheric Methane in the Hudson Bay Lowlands, Canada, *Journal of Geophysical Research: Atmospheres*, 123, 4695–4711, <https://doi.org/10.1002/2017JD027972>, 2018.



- Gloor, E., Wilson, C., Chipperfield, M. P., Chevallier, F., Buermann, W., Boesch, H., Parker, R., Somkuti, P., Gatti, L. V., Correia, C., Domingues, L. G., Peters, W., Miller, J., Deeter, M. N., and Sullivan, M. J. P.: Tropical land carbon cycle responses to 2015/16 El Niño as recorded by atmospheric greenhouse gas and remote sensing data, *Philosophical Transactions of the Royal Society B: Biological Sciences*, 373, 20170302, <https://doi.org/10.1098/rstb.2017.0302>, 2018.
- Hersbach, H., Bell, B., Berrisford, P., Hirahara, S., Horányi, A., Muñoz-Sabater, J., Nicolas, J., Peubey, C., Radu, R., Schepers, D., Simmons, A., Soci, C., Abdalla, S., Abellan, X., Balsamo, G., Bechtold, P., Biavati, G., Bidlot, J., Bonavita, M., De Chiara, G., Dahlgren, P., Dee, D., Diamantakis, M., Dragani, R., Flemming, J., Forbes, R., Fuentes, M., Geer, A., Haimberger, L., Healy, S., Hogan, R. J., Hólm, E., Janisková, M., Keeley, S., Laloyaux, P., Lopez, P., Lupu, C., Radnoti, G., de Rosnay, P., Rozum, I., Vamborg, F., Villaume, S., and Thépaut, J.-N.: The ERA5 global reanalysis, *Quarterly Journal of the Royal Meteorological Society*, 146, 1999–2049, <https://doi.org/https://doi.org/10.1002/qj.3803>, 2020.
- Huijnen, V., Williams, J., van Weele, M., van Noije, T., Krol, M., Dentener, F., Segers, A., Houweling, S., Peters, W., de Laat, J., Boersma, F., Bergamaschi, P., van Velthoven, P., Le Sager, P., Eskes, H., Alkemade, F., Scheele, R., Nédélec, P., and Pätz, H.-W.: The global chemistry transport model TM5: description and evaluation of the tropospheric chemistry version 3.0, *Geoscientific Model Development*, 3, 445–473, <https://doi.org/10.5194/gmd-3-445-2010>, 2010.
- Jacob, D. J. : 4.3.1 Buoyancy, Princeton University Press, 1999.
- Lin, X., Rogers, B. M., Sweeney, C., Chevallier, F., Arshinov, M., Dlugokencky, E., Machida, T., Sasakawa, M., Tans, P., and Keppel-Aleks, G.: Siberian and temperate ecosystems shape Northern Hemisphere atmospheric CO<sub>2</sub> seasonal amplification, *Proceedings of the National Academy of Sciences*, 117, 21079–21087, <https://doi.org/10.1073/pnas.1914135117>, 2020.
- Liu, T., Mickley, L. J., Marlier, M. E., DeFries, R. S., Khan, M. F., Latif, M. T., and Karambelas, A.: Diagnosing spatial biases and uncertainties in global fire emissions inventories: Indonesia as regional case study, *Remote Sensing of Environment*, 237, 111557, 2020.
- Lu, X., Jacob, D. J., Zhang, Y., Maasackers, J. D., Sulprizio, M. P., Shen, L., Qu, Z., Scarpelli, T. R., Nesser, H., Yantosca, R. M., Sheng, J., Andrews, A., Parker, R. J., Boesch, H., Bloom, A. A., and Ma, S.: Global methane budget and trend, 2010–2017: complementarity of inverse analyses using in situ (GLOBALVIEWplus CH<sub>4</sub> ObsPack) and satellite (GOSAT) observations, *Atmospheric Chemistry and Physics*, 21, 4637–4657, <https://doi.org/10.5194/acp-21-4637-2021>, publisher: Copernicus GmbH, 2021.
- Lunt, M. F., Palmer, P. I., Lorente, A., Borsdorff, T., Landgraf, J., Parker, R. J., and Boesch, H.: Rain-fed pulses of methane from East Africa during 2018–2019 contributed to atmospheric growth rate, *Environmental Research Letters*, 16, <https://doi.org/10.1088/1748-9326/abd8fa>, publisher: IOP Publishing, 2021.
- McNorton, J., Wilson, C., Gloor, M., Parker, R. J., Boesch, H., Feng, W., Hossaini, R., and Chipperfield, M. P.: Attribution of recent increases in atmospheric methane through 3-D inverse modelling, *Atmospheric Chemistry and Physics*, 18, 18149–18168, <https://doi.org/10.5194/acp-18-18149-2018>, 2018.
- Meirink, J. F., Bergamaschi, P., and Krol, M. C.: Four-dimensional variational data assimilation for inverse modelling of atmospheric methane emissions: method and comparison with synthesis inversion, *Atmospheric Chemistry and Physics*, 8, 6341–6353, <https://doi.org/10.5194/acp-8-6341-2008>, 2008.
- Monks, S. A., Arnold, S. R., Hollaway, M. J., Pope, R. J., Wilson, C., Feng, W., Emmerson, K. M., Kerridge, B. J., Latter, B. L., Miles, G. M., Siddans, R., and Chipperfield, M. P.: The TOMCAT global chemical transport model v1.6: description of chemical mechanism and model evaluation, *Geoscientific Model Development*, 10, 3025–3057, <https://doi.org/10.5194/gmd-10-3025-2017>, 2017.

- 645 Murguia-Flores, F., Arndt, S., Ganesan, A. L., Murray-Tortarolo, G., and Hornibrook, E. R. C.: Soil Methanotrophy Model (MeMo v1.0): a process-based model to quantify global uptake of atmospheric methane by soil, *Geoscientific Model Development*, 11, 2009–2032, <https://doi.org/10.5194/gmd-11-2009-2018>, 2018.
- Naus, S., Montzka, S. A., Patra, P. K., and Krol, M. C.: A three-dimensional-model inversion of methyl chloroform to constrain the atmospheric oxidative capacity, *Atmospheric Chemistry and Physics*, 21, 4809–4824, <https://doi.org/10.5194/acp-21-4809-2021>, 2021.
- 650 Nisbet, E. G., Dlugokencky, E. J., Manning, M. R., Lowry, D., Fisher, R. E., France, J. L., Michel, S. E., Miller, J. B., White, J. W. C., Vaughn, B., Bousquet, P., Pyle, J. A., Warwick, N. J., Cain, M., Brownlow, R., Zazzeri, G., M., L., Manning, A. C., Gloor, E., Worthy, D. E. J., Brunke, E.-G., Labuschagne, C., Wolff, E. W., and Ganesan, A. L.: Rising atmospheric methane: 2007–2014 growth and isotopic shift, *Global Biogeochemical Cycles*, 30, 1356–1370, <https://doi.org/https://doi.org/10.1002/2016GB005406>, 2016.
- Nisbet, E. G., Manning, M. R., Dlugokencky, E. J., Fisher, R. E., Lowry, D., Michel, S. E., Myhre, C. L., Platt, S. M., Allen, G., Bousquet, P., Brownlow, R., Cain, M., France, J. L., Hermansen, O., Hossaini, R., Jones, A. E., Levin, I., Manning, A. C., Myhre, G., Pyle, J. A., Vaughn, B. H., Warwick, N. J., and White, J. W. C.: Very Strong Atmospheric Methane Growth in the 4 Years 2014–2017: Implications for the Paris Agreement, *Global Biogeochemical Cycles*, 33, 318–342, <https://doi.org/https://doi.org/10.1029/2018GB006009>, 2019.
- 655 Parker, R. J., Boesch, H., McNorton, J., Comyn-Platt, E., Gloor, M., Wilson, C., Chipperfield, M. P., Hayman, G. D., and Bloom, A. A.: Evaluating year-to-year anomalies in tropical wetland methane emissions using satellite CH<sub>4</sub> observations, *Remote Sensing of Environment*, 211, 261–275, <https://doi.org/https://doi.org/10.1016/j.rse.2018.02.011>, 2018.
- 660 Parker, R. J., Wilson, C., Bloom, A. A., Comyn-Platt, E., Hayman, G., McNorton, J., Boesch, H., and Chipperfield, M. P.: Exploring constraints on a wetland methane emission ensemble (WetCHARTs) using GOSAT observations, *Biogeosciences*, 17, <https://doi.org/10.5194/bg-17-5669-2020>, publisher: Copernicus GmbH, 2020.
- Patra, P. K., Houweling, S., Krol, M., Bousquet, P., Belikov, D., Bergmann, D., Bian, H., Cameron-Smith, P., Chipperfield, M. P., Corbin, K., Fortems-Cheiney, A., Fraser, A., Gloor, E., Hess, P., Ito, A., Kawa, S. R., Law, R. M., Loh, Z., Maksyutov, S., Meng, L., Palmer, P. I., Prinn, R. G., Rigby, M., Saito, R., and Wilson, C.: TransCom model simulations of CH<sub>4</sub> and related species: linking transport, surface flux and chemical loss with CH<sub>4</sub> variability in the troposphere and lower stratosphere, *Atmospheric Chemistry and Physics*, 11, 12 813–12 837, <https://doi.org/10.5194/acp-11-12813-2011>, 2011.
- 665 Patra, P. K., Krol, M. C., Prinn, R. G., Takigawa, M., Mühle, J., Montzka, S. A., Lal, S., Yamashita, Y., Naus, S., Chandra, N., Weiss, R. F., Krummel, P. B., Fraser, P. J., O’Doherty, S., and Elkins, J. W.: Methyl Chloroform Continues to Constrain the Hydroxyl (OH) Variability in the Troposphere, *Journal of Geophysical Research: Atmospheres*, 126, e2020JD033 862, <https://doi.org/10.1029/2020JD033862>, 2021.
- 670 Peng, S., Piao, S., Bousquet, P., Ciais, P., Li, B., Lin, X., Tao, S., Wang, Z., Zhang, Y., and Zhou, F.: Inventory of anthropogenic methane emissions in mainland China from 1980 to 2010, *Atmospheric Chemistry and Physics*, 16, <https://doi.org/10.5194/acp-16-14545-2016>, 2016.
- 675 Pickers, P. A. and Manning, A. C.: Investigating bias in the application of curve fitting programs to atmospheric time series, *Atmospheric Measurement Techniques*, 8, 1469–1489, <https://doi.org/10.5194/amt-8-1469-2015>, 2015.
- Pickett-Heaps, C. A., Jacob, D. J., Wecht, K. J., Kort, E. A., Wofsy, S. C., Diskin, G. S., Worthy, D. E. J., Kaplan, J. O., Bey, I., and Drevet, J.: Magnitude and seasonality of wetland methane emissions from the Hudson Bay Lowlands (Canada), *Atmospheric Chemistry and Physics*, 11, 3773–3779, <https://doi.org/10.5194/acp-11-3773-2011>, 2011.
- 680 Prinn, R. G., Weiss, R. F., Arduini, J., Arnold, T., DeWitt, H. L., Fraser, P. J., Ganesan, A. L., Gasore, J., Harth, C. M., Hermansen, O., Kim, J., Krummel, P. B., Li, S., Loh, Z. M., Lunder, C. R., Maione, M., Manning, A. J., Miller, B. R., Mitrevski, B., Mühle, J., O’Doherty, S., Park, S., Reimann, S., Rigby, M., Saito, T., Salameh, P. K., Schmidt, R., Simmonds, P. G., Steele, L. P., Vollmer, M. K., Wang, R. H.,

- 685 Yao, B., Yokouchi, Y., Young, D., and Zhou, L.: History of chemically and radiatively important atmospheric gases from the Advanced Global Atmospheric Gases Experiment (AGAGE), *Earth System Science Data*, 10, 985–1018, <https://doi.org/https://doi.org/10.5194/essd-10-985-2018>, 2018.
- Randerson, J., Van Der Werf, G., Giglio, L., Collatz, G., and Kasibhatla, P.: Global Fire Emissions Database, Version 4.1 (GFEDv4), <https://doi.org/10.3334/ORNLDAAAC/1293>, 2017.
- 690 Rigby, M., Montzka, S. A., Prinn, R. G., White, J. W. C., Young, D., O’Doherty, S., Lunt, M. F., Ganesan, A. L., Manning, A. J., Simmonds, P. G., Salameh, P. K., Harth, C. M., Mühle, J., Weiss, R. F., Fraser, P. J., Steele, L. P., Krummel, P. B., McCulloch, A., and Park, S.: Role of atmospheric oxidation in recent methane growth, *Proceedings of the National Academy of Sciences*, 114, 5373–5377, <https://doi.org/10.1073/pnas.1616426114>, 2017.
- Sasakawa, M., Shimoyama, K., Machida, T., Tsuda, N., Suto, H., Arshinov, M., Davydov, D., Fofonov, A., Krasnov, O., Saeki, T., Koyama, Y., and Maksyutov, S.: Continuous measurements of methane from a tower network over Siberia, <https://doi.org/10.17595/20160901.004>, reference Date: 2022/10/20, 2010.
- 695 Saunio, M., Stavert, A. R., Poulter, B., Bousquet, P., Canadell, J. G., Jackson, R. B., Raymond, P. A., Dlugokencky, E. J., Houweling, S., Patra, P. K., Ciais, P., Arora, V. K., Bastviken, D., Bergamaschi, P., Blake, D. R., Brailsford, G., Bruhwiler, L., Carlson, K. M., Carrol, M., Castaldi, S., Chandra, N., Crevoisier, C., Crill, P. M., Covey, K., Curry, C. L., Etiope, G., Frankenberg, C., Gedney, N., Hegglin, M. I., Hoglund-Isaksson, L., Hugelius, G., Ishizawa, M., Ito, A., Janssens-Maenhout, G., Jensen, K. M., Joos, F., Kleinen, T., Krummel, P. B., Langenfelds, R. L., Laruelle, G. G., Liu, L., Machida, T., Maksyutov, S., McDonald, K. C., McNorton, J., Miller, P. A., Melton, 700 J. R., Morino, I., Müller, J., Murguía-Flores, F., Naik, V., Niwa, Y., Noce, S., O’Doherty, S., Parker, R. J., Peng, C., Peng, S., Peters, G. P., Prigent, C., Prinn, R., Ramonet, M., Regnier, P., Riley, W. J., Rosentreter, J. A., Segers, A., Simpson, I. J., Shi, H., Smith, S. J., Steele, L. P., Thornton, B. F., Tian, H., Tohjima, Y., Tubiello, F. N., Tsuruta, A., Viovy, N., Voulgarakis, A., Weber, T. S., van Weele, M., van der Werf, G. R., Weiss, R. F., Worthy, D., Wunch, D., Yin, Y., Yoshida, Y., Zhang, W., Zhang, Z., Zhao, Y., Zheng, B., Zhu, Q., Zhu, Q., and Zhuang, Q.: The Global Methane Budget 2000–2017, *Earth System Science Data*, 12, 1561–1623, <https://doi.org/10.5194/essd-12-1561-2020>, 705 2020.
- Scarpelli, T. R., Jacob, D. J., Moran, M., Reuland, F., and Gordon, D.: A gridded inventory of Canada’s anthropogenic methane emissions, *Environmental Research Letters*, 17, 014007, <https://doi.org/10.1088/1748-9326/ac40b1>, publisher: IOP Publishing, 2021.
- Spivakovsky, C. M., Logan, J. A., Montzka, S. A., Balkanski, Y. J., Foreman-Fowler, M., Jones, D. B. A., Horowitz, L. W., Fusco, A. C., Brenninkmeijer, C. A. M., Prather, M. J., Wofsy, S. C., and McElroy, M. B.: Three-dimensional climatological distribution of tropospheric OH: Update and evaluation, *Journal of Geophysical Research: Atmospheres*, 105, 8931–8980, <https://doi.org/https://doi.org/10.1029/1999JD901006>, 2000.
- 710 Stavert, A. R., Saunio, M., Canadell, J. G., Poulter, B., Jackson, R. B., Regnier, P., Lauerwald, R., Raymond, P. A., Allen, G. H., Patra, P. K., Bergamaschi, P., Bousquet, P., Chandra, N., Ciais, P., Gustafson, A., Ishizawa, M., Ito, A., Kleinen, T., Maksyutov, S., McNorton, J., Melton, J. R., Müller, J., Niwa, Y., Peng, S., Riley, W. J., Segers, A., Tian, H., Tsuruta, A., Yin, Y., Zhang, Z., Zheng, B., and Zhuang, 715 Q.: Regional trends and drivers of the global methane budget, *Global Change Biology*, 28, <https://doi.org/10.1111/gcb.15901>, 2022.
- Thoning, K. W., Tans, P. P., and Komhyr, W. D.: Atmospheric carbon dioxide at Mauna Loa Observatory: 2. Analysis of the NOAA GMCC data, 1974–1985, *Journal of Geophysical Research: Atmospheres*, 94, 8549–8565, <https://doi.org/https://doi.org/10.1029/JD094iD06p08549>, 1989.

- Tohjima, Y., Machida, T., Utiyama, M., Katsumoto, M., Fujinuma, Y., and Maksyutov, S.: Analysis and presentation of in situ atmospheric methane measurements from Cape Ochi-ishi and Hateruma Island, *Journal of Geophysical Research: Atmospheres*, 107, ACH 8–1–ACH 8–11, <https://doi.org/https://doi.org/10.1029/2001JD001003>, 2002.
- Turner, A. J., Frankenberg, C., Wennberg, P. O., and Jacob, D. J.: Ambiguity in the causes for decadal trends in atmospheric methane and hydroxyl, *Proceedings of the National Academy of Sciences*, 114, 5367–5372, <https://doi.org/10.1073/pnas.1616020114>, 2017.
- van der Werf, G. R., Randerson, J. T., Giglio, L., van Leeuwen, T. T., Chen, Y., Rogers, B. M., Mu, M., van Marle, M. J. E., Morton, D. C., Collatz, G. J., Yokelson, R. J., and Kasibhatla, P. S.: Global fire emissions estimates during 1997–2016, *Earth System Science Data*, 9, 697–720, <https://doi.org/10.5194/essd-9-697-2017>, 2017.
- Weber, T., Wiseman, N. A., and Kock, A.: Global ocean methane emissions dominated by shallow coastal waters, *Nature Communications*, 10, 4584, <https://doi.org/10.1038/s41467-019-12541-7>, 2019.
- Wilson, C., Chipperfield, M. P., Gloor, M., and Chevallier, F.: Development of a variational flux inversion system (INVICAT v1.0) using the TOMCAT chemical transport model, *Geoscientific Model Development*, 7, 2485–2500, <https://doi.org/10.5194/gmd-7-2485-2014>, 2014.
- Wilson, C., Gloor, M., Gatti, L. V., Miller, J. B., Monks, S. A., McNorton, J., Bloom, A. A., Basso, L. S., and Chipperfield, M. P.: Contribution of regional sources to atmospheric methane over the Amazon Basin in 2010 and 2011, *Global Biogeochemical Cycles*, 30, 400–420, <https://doi.org/https://doi.org/10.1002/2015GB005300>, 2016.
- Wilson, C., Chipperfield, M. P., Gloor, M., Parker, R. J., Boesch, H., McNorton, J., Gatti, L. V., Miller, J. B., Basso, L. S., and Monks, S. A.: Large and increasing methane emissions from eastern Amazonia derived from satellite data, 2010–2018, *Atmospheric Chemistry and Physics*, 21, 10 643–10 669, <https://doi.org/10.5194/acp-21-10643-2021>, 2021.
- Zhao, Y., Sauniois, M., Bousquet, P., Lin, X., Berchet, A., Hegglin, M. I., Canadell, J. G., Jackson, R. B., Hauglustaine, D. A., Szopa, S., Stavert, A. R., Abraham, N. L., Archibald, A. T., Bekki, S., Deushi, M., Jöckel, P., Josse, B., Kinnison, D., Kirner, O., Marécal, V., O’Connor, F. M., Plummer, D. A., Revell, L. E., Rozanov, E., Stenke, A., Strode, S., Tilmes, S., Dlugokencky, E. J., and Zheng, B.: Inter-model comparison of global hydroxyl radical (OH) distributions and their impact on atmospheric methane over the 2000–2016 period, *Atmospheric Chemistry and Physics*, 19, 13 701–13 723, <https://doi.org/10.5194/acp-19-13701-2019>, 2019.

**Table 1.** List of 22 NOAA Sites used in the analysis (Dlugokencky et al., 2021).

Site Name	Latitude (° North)	Longitude (° East)	Site Code
Alert, Canada	82.45	-62.50	ALT
Ny-Alesund, Svalbard	78.91	11.80	ZEP
Barrow, Alaska, USA	71.32	156.60	BRW
Storhofdi, Vestmannaeyjar, Iceland	63.40	-20.28	ICE
Mace Head, Ireland	53.32	-9.90	MHD
Ulaan Uul, Mongolia	44.45	111.09	UUM
Niwot Ridge, Colorado, USA	40.05	-105.63	NWR
Terceira Island, Azores	38.70	-27.35	AZR
Mt Waligaun, Peoples Republic of China	36.27	100.92	WLG
Tudor Hill, Bermuda	32.26	-64.87	BMW
Izana, Tenerife	28.30	-16.48	IZO
Sand Island, Midway	28.22	-177.37	MID
Mauna Loa, Hawaii, USA	19.53	-155.58	MLO
Cape Kumukahi, Hawaii, USA	19.52	-154.82	KUM
Mariana Islands, Guam	13.39	144.65	GMI
Ragged Point, Barbados	13.17	-59.43	RPB
Mahe Island, Seychelles	-4.68	55.53	SEY
Ascension Island, UK	-7.97	-14.40	ASC
Tutuila, American Samoa	-14.25	-170.56	SMO
Palmer Station, Antarctica	-64.92	-64.00	PSA
Syowa Station, Antarctica	-69.00	39.57	SYO
South Pole, Antarctica	-89.98	-24.80	SPO

**Table 2.** List of 18 regions and their region code for each tracer.

Region Code	Region Name
AUS	Australasia
CAFR	Central Africa
CAN	Canada
CHJA	China & Japan
EBRA	East Brazil
EUR	Europe
INBA	India & Bangladesh
ME	Middle East
NAFR	North Africa
NAM	North America
NASA	Non-Amazon South America
NBRA	North Brazil
NOA	North Oceans & Arctic
RUS	Russia
SAFR	South Africa
SBRA	South Brazil
SEA	South East Asia
SOA	South Oceans & Antarctica

**Table 3.** List of the difference TOMCAT simulations.

TOMCAT Simulation	Experiment
TOM_regional	Regional tagged tracer simulation
TOM_transport	Investigating changes in transport
TOM_one	Background sensitivity - One month decay rate
TOM_twelve	Background sensitivity - Twelve month decay rate

**Table A1.** A table comparing the results  $\Delta$ SCA (ppb) of TOM\_regional, TOM\_transport, TOM\_twelve and TOM\_one simulations.

Tagged Tracers	TOM_regional	TOM_transport	TOM_twelve	TOM_one
Total (sum of all tracers)	-6.38	-2.09	-6.38	-6.38
Sum of Regions	3.54	0.23	3.43	-2.61
Background	-9.93	-2.32	-9.81	-3.74
Canada	-2.97	0.24	-2.91	-4.09
Middle East	-2.13	-0.22	-2.14	-0.95
Europe	-1.48	0.76	-1.5	1.43
Russia	2.71	-0.60	2.67	1.56
North America	2.46	-0.91	2.52	0.52